

## ABSTRACT

Title of Thesis: PERFORMANCE OF LINK SLAB USING  
ECC AND UHPC

Naiyi Li, Master of Science, 2019

Thesis directed by: Professor Chung C. Fu  
Department of Civil and Environmental  
Engineering

Conventional bridge design has been challenged by durability and reliability issues due to expansion joints. Chloride-contaminated infiltration and debris accumulation in traditional expansion joints affect the bridge performance negatively. Link slab has emerging as an effective alternative in bridge rehabilitation and design by eliminating expansion joints while the bridge structure remains simply supported. Engineered Cementitious Composites (ECC) and Ultra-High Performance Concrete (UHPC) are desired material in link slab application due to their high strength and tensile ductility. Presented in this thesis is a research project conducted by the BEST center at the University of Maryland to study link slab application with UHPC and ECC. Two bridge models were generated for finite element analysis. In addition, a field test was prepared. Experiments were carried out to study material properties of ECC and UHPC for a preliminary assessment of link slab performance using these materials. Results found that ECC and UHPC are adequate for link slab for their strength, high tensile ductility and fine cracks development.

PERFORMANCE OF LINK SLAB USING ECC AND UHPC

by

Naiyi Li

Thesis submitted to the Faculty of the Graduate School of the  
University of Maryland, College Park, in partial fulfillment  
of the requirements for the degree of  
Master of Science  
2019

Advisory Committee:  
Dr. Chung C. Fu, Chair  
Dr. Allison C. Reilly  
Dr. Brian M. Phillips

© Copyright by  
Naiyi Li  
2019

## Dedication

I am dedicating this thesis to my family for the all supports I received. A special feeling of gratitude to my parents, Huang and Li whose encouragements have meant and continue to mean so much to me. My wife, Jingyao, has been supporting me throughout the process. The completion of my thesis would not have been possible without the support of her.

I also dedicate this thesis to my friends who have helped and supported me. I will always appreciate what they have done.

## Acknowledgements

I wish to thank my committee members who were generous with their expertise and precious time. A special thanks to Dr. Chung C. Fu, my committee chairman for his willingness and generosity to provide me an opportunity to do the research as a master student. Without his support and guidance, I would not be able to complete my master's degree. I will be forever thankful to you. Thank you, Dr. Allison Reilly and Dr. Brian M. Phillips for agreeing to serve on my committee.

I would like to extend my sincere thanks to my peers at the BEST center. Many thanks to Kuang-Yuan Hou, Yifan Zhu and Xinya Liu, whom I had great pleasure of working with. Thanks very much for the assistance and guidance everyone have provided. It is sincerely appreciated.

I would like to acknowledge and thank the Civil and Environmental Engineering Department for providing me the opportunity to conduct my research and pursuit my goals. Special thanks go to the members of staff of the department.

# Table of Contents

List of Tables .....	vi
List of Equations .....	vi
List of Figures .....	vii
List of Abbreviations .....	viii
Chapter 1 Introduction .....	1
1.1 Motivation and Introduction .....	1
1.2 Scope .....	2
1.3 Objective .....	3
Chapter 2 Literature Review .....	4
2.2 Literature Review on Materials .....	4
2.2.1 Victor Li 2008 .....	4
2.1.2 Manish A. Kewalramani et al. 2016 .....	7
2.1.3 Oguz Gunes et al. 2012 .....	10
2.2. Literature Review on Link Slab .....	13
2.2.1 Caner and Zia 1998 .....	13
2.2.2 Alexander Au, Clifford Lan, Jim Au and Bala Tharmmabala 2013 .....	16
2.3.3 Kenneth M. Wing and Meryyn J. Kowalsky 2005 .....	19
Chapter 3 Experiments .....	26
3.1 Objective and overview .....	26
3.2 Materials and expectations .....	26
3.2.1 UHPC .....	26
3.2.2 ECC .....	27
3.2.3 Expectation .....	27
3.3 Testing .....	28
3.3.1 Sensor information .....	28
3.3.2 Sensor installation .....	29
3.3.3 Procedure .....	31
Chapter 4 Finite Element Analysis .....	35
4.1 Description .....	35
4.2 Bridge Details .....	36
4.3 Finite Element Model using ANSYS Workbench® .....	38
4.3.1 Overview .....	38
4.3.2 Results for Modal Analysis .....	39
4.4 Finite Element Model using CSiBridge® .....	41
4.4.1 Overview .....	41

4.4.2 Shell Elements vs. Solid Elements.....	42
4.4.3 Results for Modal Analysis.....	43
4.4.4 Structural Response for Moving Truck Loads.....	45
4.6 Modal Analysis Comparison.....	48
Chapter 5 Field Test.....	49
5.1 Description.....	49
5.1.1 Strain Distribution.....	49
5.1.2 Sensor System Configuration .....	50
5.2 Preparation .....	50
5.3 Equipment.....	52
5.4 Procedure .....	54
Chapter 6 Results .....	55
6.1 Results for ECC and UHPC.....	55
6.1.1 Data Processing.....	55
6.1.2 Maximum compressive strength.....	56
6.1.3 Maximum tensile strain.....	58
6.1.4 Stress vs. Strain Curve .....	60
6.2 Results on Sensor Performance .....	67
6.2.1 Sensor Performance Criteria .....	67
6.2.2 Sensor Survival Rates .....	67
6.2.3 Sensor Failure Due to Lost Connection.....	69
6.2.4 Sensor Failure when reaching a certain level of strain .....	69
6.2.5 Complete Sensor Failure.....	70
6.2.6 Possible Causes for Sensor Disturbance and Failures .....	71
6.2.7 Recommendation on Sensor Application.....	72
6.3 Fine Crack Development .....	74
Chapter 7 Discussion .....	77
7.1 Lab Test .....	77
7.2 Sensor Protection .....	78
7.3 Evaluation of Sensor Performance.....	79
Chapter 8 Conclusion and Future Work .....	80
8.1 Conclusion .....	80
8.2 Future Work.....	82
Appendix: Bridge Thermal Analysis .....	84
Bibliography .....	101

## List of Tables

Table 2.1: Typical ECC mix design (Li, 2008) .....	5
Table 3.1: Sensor distributions .....	32
Table 3.2: Updated ECC mixture.....	33
Table 4.1: Modal frequencies by Ansys Workbench® .....	39
Table 4.2: Modal frequencies by CSiBridge® .....	43
Table 4.3: Modal analysis comparison .....	48
Table 6.1: Maximum compressive strength.....	56
Table 6.2: Sensor failure and survival rates .....	68
Table 6.3: Strain level of lost compatibility.....	73

## List of Equations

Equation 2.1 .....	15
Equation 2.2 .....	17
Equation 2.3 .....	17
Equation 2.4 .....	17
Equation 2.5 .....	23
Equation 2.6 .....	23
Equation 2.7 .....	23
Equation 2.8 .....	24
Equation 2.9 .....	24
Equation 2.10 .....	25
Equation 2.11 .....	25
Equation 6.1 .....	65
Equation 6.2 .....	66
Equation 6.3 .....	66

## List of Figures

Figure 2.1: “Metal-like” behavior of ECC (Li, 2008) .....	7
Figure 2.2: Tensile strength reduction of PVA fibers (Magalhães et al. 2013) .....	8
Figure 2.3: ECC link slab in a bridge in Michigan, USA (Magalhães et al. 2013) .....	9
Figure 2.4: UHPC compared with normal concrete (Gunes & Ulm et al. 2012).....	11
Figure 2.5: Typical jointless bridge configuration (Caner & Zia, 1998) .....	15
Figure 2.6: Debonded link slab system (Alexander Au, et al 2013).....	16
Figure 2.7: Link slab crack pattern (Alexander Au, et al 2013) .....	18
Figure 2.8: NCDOT link slab rehabilitation design (Wing & Kowalsky, 2005).....	21
Figure 3.1: Strain Gauge SenSpot™ Sensor.....	29
Figure 3.2: Sensor installation on a bridge girder.....	29
Figure 3.3: Strain gauge installation on a metal plate.....	31
Figure 3.4: Three-point bending test apparatus (ASTM C78/C78M-18) .....	33
Figure 3.5: Link slab specimen with strain gauge .....	34
Figure 4.1: Plan view of bridge CEX952001.....	37
Figure 4.3: Bridge model geometry in Ansys Workbench® .....	38
Figure 4.5: Tet10, Hex20 and Wed15 elements in Ansys Workbench® .....	40
Figure 4.6: Total deformation in dynamic analysis .....	40
Figure 4.7: 1st modal shape, $f = 2.53$ Hz .....	40
Figure 4.8: 2nd modal shape, $f = 2.72$ Hz.....	41
Figure 4.9: 3rd modal shape, $f = 3.58$ Hz .....	41
Figure 4.10: CSiBridge® model using shell elements.....	42
Figure 4.11: 1st mode shape, $f = 2.46$ Hz .....	43
Figure 4.12: 2nd mode shape, $f = 2.65$ Hz.....	44
Figure 4.12: 3rd mode shape, $f = 3.66$ Hz .....	44
Figure 4.13: HS20-44 vehicle load per AASHTO specifications .....	45
Figure 4.14: Moving truck loads visualization .....	46
Figure 4.15: Maximum and minimum vertical shear envelop .....	46
Figure 4.16: Maximum moment envelop.....	47
Figure 4.17: Maximum vertical deflection .....	48
Figure 5.1: Strain distribution of link slab .....	49
Figure 5.2: Plan view of sensor locations .....	51
Figure 5.3: Elevation view of sensor location on UHPC link slab .....	51
Figure 5.4: Elevation view of sensor location on ECC link slab .....	52
Figure 5.5: Sensor system with a steel plate .....	53
Figure 5.6: Solar powered DAQ .....	53

Figure 5.7: Network of data collection .....	54
Figure 6.1: ECC compressive strength .....	58
Figure 6.2: Maximum concrete tensile strain .....	59
Figure 6.3: Maximum steel tensile strain.....	60
Figure 6.4: Cyclic loading pattern of specimen No. 14 (UHPC).....	61
Figure 6.5: Stresses of specimen 14 (UHPC) .....	61
Figure 6.6: Strains of specimen No. 14 (UHPC) .....	62
Figure 6.7: Cyclic applied loads for specimen No.7 (ECC) .....	63
Figure 6.8: Stresses on specimen No. 7 (ECC).....	63
Figure 6.9: Strain in first 3 loading cycles (ECC) .....	64
Figure 6.10: Strain in 4th and 5th loading cycles (ECC).....	64
Figure 6.11: Stress-strain curve for the 2nd loading cycle .....	65
Figure 6.12: Stress-strain curve for the 3rd loading cycle .....	66
Figure 6.13: Stress-strain curve for the 4th loading cycle .....	66
Figure 6.15: Temporary loss of connection in sensors .....	69
Figure 6.16: Temporary loss of compatibility .....	70
Figure 6.17: Compatibility between sensors recovered.....	70
Figure 6.19: Point of lost compatibility .....	72
Figure 6.20: Fine cracks on an ECC specimen.....	75
Figure 6.21: Fracture plane formed by fine cracks on a UHPC specimen .....	75
Figure 6.22: Fracture plane formed by multiple fine cracks (ECC) .....	76
Figure 7.1: Thin slab showing ECC tensile ductility .....	77
Figure 7.2: Overall sensor survival rate .....	79
Figure 7.3: Survival rate by configuration.....	79

## List of Abbreviations

SD: Structurally deficient .....	1
MDTA: Maryland Transportation Authority .....	2
BEST: Bridge Engineering Software and Technology .....	2
ECC: Engineered Cementitious Composites .....	2
UHPC: Ultra-High Performance Concrete .....	2
MTO: Ministry of Transportation of Ontario .....	16
DLS: Debonded link slab system.....	19

# Chapter 1 Introduction

## 1.1 Motivation and Introduction

Bridges serve an essential role in the infrastructure system to create links between two points. Demands on improving bridge performance and reliability keep growing as the population and the size of communities increase. Unlike regular roads, there are fewer substitutes in bridges in terms of transportation alternatives. Hence, a failure in a bridge could cause massive loss for the community it serves. In fact, the 2017 ASCE Infrastructure Report Card graded the overall condition of bridges as C+ in the United States. According to the report, approximately 40% of the bridges in the United States are at least 50 years old and more bridges are approaching their design life. Worse, 9.1% of the bridges in the nation are rated as structurally deficient (SD), while it was approximated that 188 million trips are on these bridges every day. Therefore, rehabilitation and innovation in bridge engineering are urgent and the current estimated cost for bridge rehabilitation across the country is \$123 billion.

In bridge engineering, it is common to design bridges as simply-supported structures by connecting each span with expansion joints. Yet, the use of expansion joints allows penetration of chloride-contaminated water and debris accumulation that affect the joints significantly over time, which led to high cost in bridge maintenance and rehabilitation. This type of problem is more common in older bridges as corrosion has been taking place for an extended period of time. In recent years, link slab has emerged to become an advantageous approach in problem solving avoiding

complicated negative moment connection design. Application of link slab eliminates traditional expansion joints by creating a jointless bridge while keeping the spans simply supported. By connecting the adjacent concrete slabs with a link slab, damages associated with water penetration, corrosion and debris accumulation can be significantly reduced and alleviated to make bridges more sustainable.

In this paper, a research project sponsored by the Maryland Transportation Authority (MDTA) was conducted by the Bridge Engineering Software and Technology (BEST) Center at the University of Maryland to investigate link slab application using two types of materials: Engineered Cementitious Composites (ECC) and Ultra-High Performance Concrete (UHPC). Both ECC and UHPC are fiber-reinforced concrete materials and they offer high strength and tensile ductility, along with ability to develop fine cracks. The material properties of ECC and UHPC are suitable for link slab design as the high strength and tensile ductility ensure the durability and reliability of the structural member. In addition, fine cracks are more efficient compared to expansion joints because a very limited amount of water would be able to penetrate through the link slab so the supporting girders and other substructures can be better protected.

## **1.2 Scope**

The project will study material properties of ECC and UHPC materials in a concrete testing facility. 14 specimens are to be casted using ECC and UHPC and will be subjected to three-point bending test following ASTM C78/C78M-18. Sensor

performance will be evaluated for recommendations in future application. In addition, two finite element models are to be generated to serve as the baseline of bridge performance in which only the super-structure is modeled. This research project also serves as a pilot project for the future field test scheduled to be performed on a typical overpass bridge in Maryland Transportation Authority (MDTA) highway system.

### **1.3 Objective**

The goal of this project is to obtain a better understanding of Engineered Cementitious Composites (ECC) and Ultra-High Performance Concrete (UHPC) in terms of their application on link slab. The high compressive and tensile strength of the two fiber-reinforced materials are to be verified. Also, the high tensile ductility of ECC and UHPC will be examined as this is critical in link slab performance.

Meanwhile, structural response of ECC and UHPC need to be monitored against cyclic loadings. Structural members on bridges are constantly subjected to repeated loads due to traffic, hence, it is important for ECC and UHPC to accommodate this effect by providing structural response that is independent to the amount of cycles that the link slab has gone through over its life span. Furthermore, the effects on ECC and UHPC in link slab applications will be studied by analyzing the test results. In addition to material properties, sensor performance is also investigated in order to study sensor properties and limit states. Therefore, recommendations can be proposed for future testing and long-term monitoring. A plan for future field test on an actual bridge is also to be carried out.

## **Chapter 2 Literature Review**

### **2.2 Literature Review on Materials**

#### **2.2.1 Victor Li 2008**

Dr. Li at the University of Michigan, Ann Arbor published an article documented recent studies on engineered cementitious composites in 2008. The study on fiber reinforced concrete dated back to the 1960's by Romauldi and co-workers (e.g. Romauldi and Batson, 1963; Romauldi and Mandel, 1964). But it was not until the 1980's when the interest in this topic became prevailed. In fact, techniques on the engineered cementitious composites keep developing over the years and there were applications of the ECC material on real structure in Japan, Europe and the US. By definition, ECC is defined as a group of materials whose tensile strength and ductility can be modified to meet certain requirements (Li, 2008). In addition, ECC usually brings high tensile strength and fine cracking patterns. Typical fiber used in ECC includes PVA, polyethylene and polypropylene fibers.

The most essential characteristics of ECC is the high tensile ductility that offers a metal-like behavior as the material approaches the inelastic region. This behavior is similar to that of a yield point on a metallic material. Meanwhile, the first microcrack will appear on the specimen. Behavior of ECC beyond this point can be classified as strain-hardening if the applied load keeps increasing. The material reaches its failure state when the fine cracks form a fracture plane. Then, ECC shows similar characteristics as normal fiber-reinforced concrete by showing a strain-

softening behavior. The high tensile ductility of ECC is extremely valuable in improving the overall structural performance by providing a larger capacity in load, deformation and energy absorption. Consequently, ECC helps to improve structural safety. A typical mix design of ECC is shown in Table 2.1.

**Table 2.1: Typical ECC mix design (Li, 2008)**

Mix Designation	Cement	Fly Ash	Sand	Water	HRWR*	Fiber (Vol %)
M45	1.0	1.2	0.8	0.56	0.012	0.02

Despite its high tensile strength and ductility, ECC is similar to normal high strength concrete in compression. Typical compressive strength of ECC varies from 30Mpa to 90Mpa (4351psi to 13052psi). The elastic modulus ranges from 20-25GPa. Strain capacity of ECC is 0.45%-0.65%, which is slightly higher than normal concrete.

Tensile ductility of ECC can be understood by studying its behavior under flexural condition. The material develops microcracking when subjected to bending and allows the specimen to experience a deformation with large curvature. This scenario makes the ECC material similar to a metal what can be bent with large deformation without failure. As a result, ECC is able to offer a range of 10-15MPa in flexural strength. Studies had shown that this behavior is instinct to ECC, regardless of the geometry of the specimen. Besides, ECC is advantageous over normal concrete materials on fatigue response (Suthiwarapirak et al, 2002).

Durability of ECC was also examined to achieve adequate serviceability on structures. Due to its high tensile ductility, ECC is expected to be used in situations where large deformation is present. A series of studies was carried out to investigate

its durability under various environment including freeze-thaw and hot-wet cycles, chloride immersion, deicing salt exposure and alkali-silicate reaction resistance (Li, 2005). Results supported that ECC is able to pass durability requirements by developing microcracks along the specimens, this is an important aspect in the application of link slab on bridges.

It was summarized that the most unique benefit of ECC is the capability of a high tensile ductility which is several hundred times great than normal concrete materials. Meanwhile, ECC is able to provide high compressive strength similar to high strength concrete. ECC behaves similarly to a metal under bending, where the material undergoes deformation with large curvature while maintaining its functionality without fracture. The metal-like behavior can be seen in Figure 2.2. This property does not rely on increasing fiber content. Thus, it makes ECC more economical in mass production and construction projects. In addition, large deformation capability of ECC creates load sharing relationship between the material and steel rebars, making the rebars in ECC members more efficient. Besides, ECC tends to develop fine cracks along the member. The crack width is generally small enough to protect the reinforcing bars or any structural members in the substructure. This is a critical aspect in link slab application because one of the goals is to alleviate corrosion in substructure caused by chloride-contaminated water.



**Figure 2.1: “Metal-like” behavior of ECC (Li, 2008)**

### **2.1.2 Manish A. Kewalramani et al. 2016**

The Abu Dhabi University had conducted a study on engineered cementitious composites (ECC) in recent years to provide insights on development and current application of the material.

The recommended maximum temperature is 50 degree Celsius to achieve service condition of ECC, below which more than 95% of the material strength can be maintained for over 100 years. A recent study (Magalhães et al. 2013) discovered that PVA fibers, which is one of the common reinforcing fibers used in ECC, showed

a massive reduction in tensile strength when the temperature increases from 90 degree Celsius to 250 degree Celsius. The result is presented in Figure 2.3. The figure indicates that the tensile strength of PVA fibers dropped 83% compared to samples that remained in normal service temperature as the temperature increased from 90 degree Celsius to 250 degree Celsius.

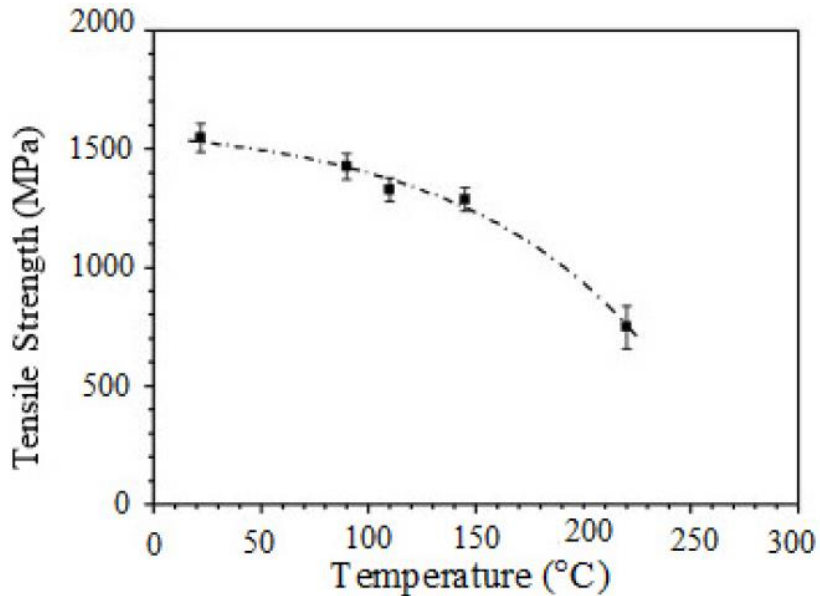


**Figure 2.2: Tensile strength reduction of PVA fibers (Magalhães et al. 2013)**

Another advantage of ECC is the effectiveness in self-healing ability in wet-dry cycles (Yang et al, 2009). In addition, resonant frequency (RF) can be used to measure the healing process by quantifying the recovery of the material's mechanical properties. Experimental results supported that the intrinsic autogenous healing of ECC allows the material to automatically repair itself from cracks. However, proper healing process demands desired temperature condition because high temperature could led to crack formation during the self-repair process.

ECC has become more frequently used in structural applications in the recent decades on building, transportation, bridges and more. The high tensile strength and high tensile ductility make the material advantageous over normal concrete in various aspects. Specifically, structural rehabilitation projects utilizes ECCs to achieve improvements over previous repair methods. Link slab, for example, is a great example where ECC has been implementing on bridges to replacing expansion joints, which tend to raise concern over water-related corrosion and debris accumulation that impact the serviceability of the bridge. The high tensile ductility prevents ECC from fracture under reparative service loadings on bridges and it is easier to be repair compared to conventional expansion joints. Figure 2.4 presents an example of ECC link slab on a bridge structure.

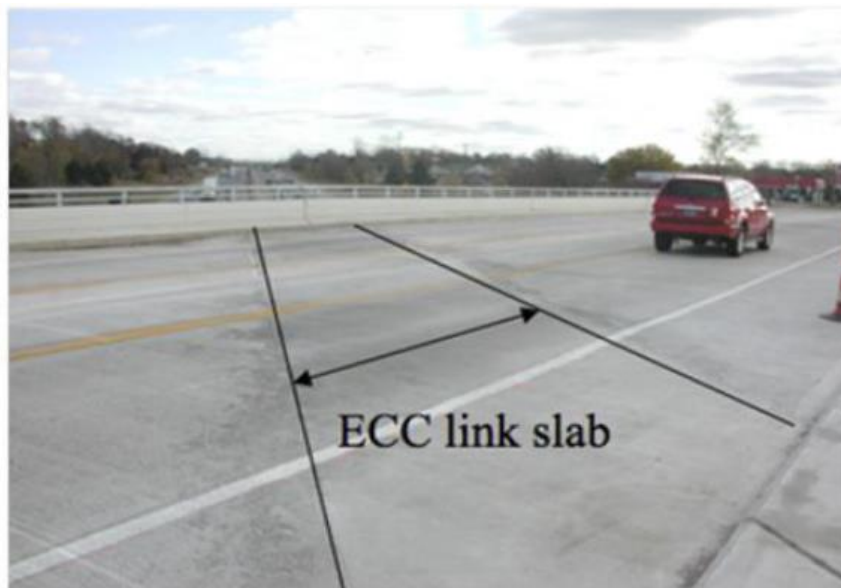


**Figure 2.3: ECC link slab in a bridge in Michigan, USA (Magalhães et al. 2013)**

### **2.1.3 Oguz Gunes et al. 2012**

A research conducted by the Cankaya University, Atilim University and the Massachusetts Institute of Technology was dedicated to study material modeling of UHPC material and investigate design approach of bridge using UHPC. UHPC stands for ultra-high-performance concrete and represents a new group of materials being developed to solve problems including durability, sustainability, load capacity, economy and environment impact of bridge structures.

UHPC has been considered as a desired solution for current challenges in bridge rehabilitation and design. It is a fiber-reinforced concrete material that consist of Portland cement, silica fume, mineral fillers, fine silica sand, superplasticizer, water and steel fibers. A typical UHPC material is able to provide compressive strength up to 200 MPa (29 ksi) and a ductile tensile strength ranges from 10-15 MPa (1.5-2.2 ksi). Members made of UHPC are capable of sustain flexural and tensile loads and dissipate the energy even when the initial cracking take places. UHPC is significantly more ductile than normal concrete so members made of UHPC do not require passive reinforcement. Combining with its high strength which allows smaller section sizes, the cost of construction can be reduced. In addition, UHPC allows structural members to have long spans, satisfying serviceability and environmental standards. At last, UHPC has a low porosity and permeability, which improves the member's resistance to water-related corrossions. Figure 2.4 shows a comparison of UHPC and normal concrete.

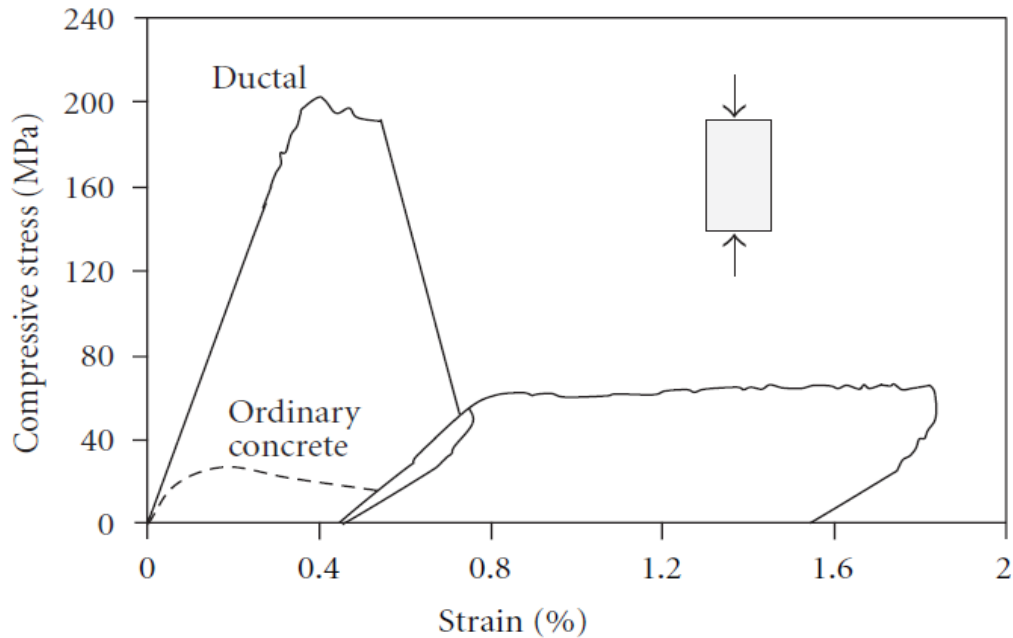


**Figure 2.4: UHPC compared with normal concrete (Gunes & Ulm et al. 2012)**

UHPC had been used in a number of bridge construction projects, with the first application being the Bourg l'es Valence bypass in Drôme in France (2002). The Federal Highway Administration (FHWA) had done researches on UHPC and concluded that the material had shown great flexural and shear capacity even with the absence of passive reinforcement and shear stirrups. To achieve this, UHPC relies on the optimized mixture between the high-strength concrete and reinforcing fibers. When this condition is met, stress on concrete can be transferred to the high-strength fibers, resulting in high tensile strength and ductile behavior.

By far, despite numerous advantages of UHPC, a number of topics need to be further studied before this material can be used in more conventional projects in the industry. Although UHPC is able to reduce the cost and labor by providing a high

strength, longer span and reduced section size, the cost for production of this material is high compared to that of a normal concrete. Due to the fact that UHPC is a relatively new concept being introduced to the industry, there is a lack of knowledge dealing with production and handling process, as well as codes and specifications to adept the material to conventional projects. Consequently, structures utilizing UHPC are mostly pilot projects that still rely on normal configuration of bridges, where the full potential of UHPC has not yet been fulfilled. While research done by the Federal Highway Administration (FHWA) indicated that a modified geometry is much more efficient in utilizing the material properties of UHPC.

The article concluded that UHPC is promising in further development of bridge structures. The high strength and ductile behavior of UHPC opens more alternatives for innovated and optimized shapes. Elimination or reduction in passive reinforcements also helps making the bridge lighter and easier to be built. Flexibility of the material allows the potential of UHPC to be mixed with other advanced composite materials, such as fiber reinforced polymers (FRP), to further innovate building materials for bridge construction. Overall, UPHC is a class of cementitious concrete materials with great potential, which still requires more effort to be unveiled and fully utilized.

## **2.2. Literature Review on Link Slab**

### **2.2.1 Caner and Zia 1998**

In 1998 Dr. Caner and Dr. Zia (Caner and Zia, 1998) conducted a test program in effort of studying behavior of link slab and offering a proposed design method for link slab. The research was motivated by improving bridge performance and reduce maintenance cost due to chloride-containment water infiltration and derris accumulation in bridge expansion joints.

The study identified the bridge deck joints as a critical problem in bridge maintenance and has been troubling engineers for decades. Hence, the idea of a jointless deck was proposed. The article pointed out that although fine cracks would still be developed on the link slabs after replacement and water could penetrate, it was still a desired condition compared to that of a jointed deck (Caner and Zia, 1998). An effective way to construct a jointless bridge is to make the slab decks continuous, meanwhile, keeping the supporting girders as simple-spans. This avoid excessive deck reinforcement. Link slab is defined as the portion of materials connecting the two adjacent steel girders. In fact, simple-span jointless bridge had already been used in many applications and two examples can be seen in Figure 2.5.

The test was performed on a steel bridge and a concrete bridge. Results and conclusion yield that the strains in both the link slab and the supporting girders were independent from different support (bearing) conditions, for example, roller or pin. And this result was only valid within the elastic region. Due to negligible stiffness of the link slab compared to the steel girders, the continuity provided by the link slab

could be omitted, leaving the girders remain as simple-span. This was verified by comparing the theoretical and test results. Experimental results indicated that the link slab tend to fail in bending instead of tension, where the top portion failed in cracking and the bottom face failed in crushing. Furthermore, this research suggested that it is reasonable to design girders independently as a simple-span configuration due to the fact that link slabs introduce negligible continuity to the bridge. Hence, designing a jointless bridge with link slab was feasible (Caner and Zia, 1998).

Caner and Zia also proposed a simple design method for jointless bridge deck using deboned link slab (Caner and Zia, 1998): Ignore the effect of link slab due to its negligible flexural stiffness compared the supporting girders. Thus, design each span separately as simply-supported structures.

Create a 5% debonded zone between the link slab and the girders to further reduce the stiffness of the link slab.

Consider the girders are simply-supported and calculate the maximum end rotations due to service loads. Transfer the rotations to link slabs and determine the corresponding moments  $M_a$ . Calculate the reinforcement needed to resist moment  $M_a$  using gross section property of the link slab. Use conservative working stress for the link slab, for instance, 40% of the yield strength of the reinforcing bars.

Limit crack width on link slab with the crack control specifications of AASHTO. The maximum crack width is defined as 0.013 inches on the link slab. The crack control criteria is expressed in Equation 2.1.

$$Z \leq f_s(d_c A)^{\frac{1}{3}} \quad (2.1)$$

Where

$$Z \leq 143 \frac{\text{kips}}{\text{in}}$$

$f_s$  = reinforcement stress in ksi

$d_c$  = concrete cover measured from extreme tension fiber to  
centriod of nearest reinforcement level in in.

$A$  = effective area per bar in sq in.

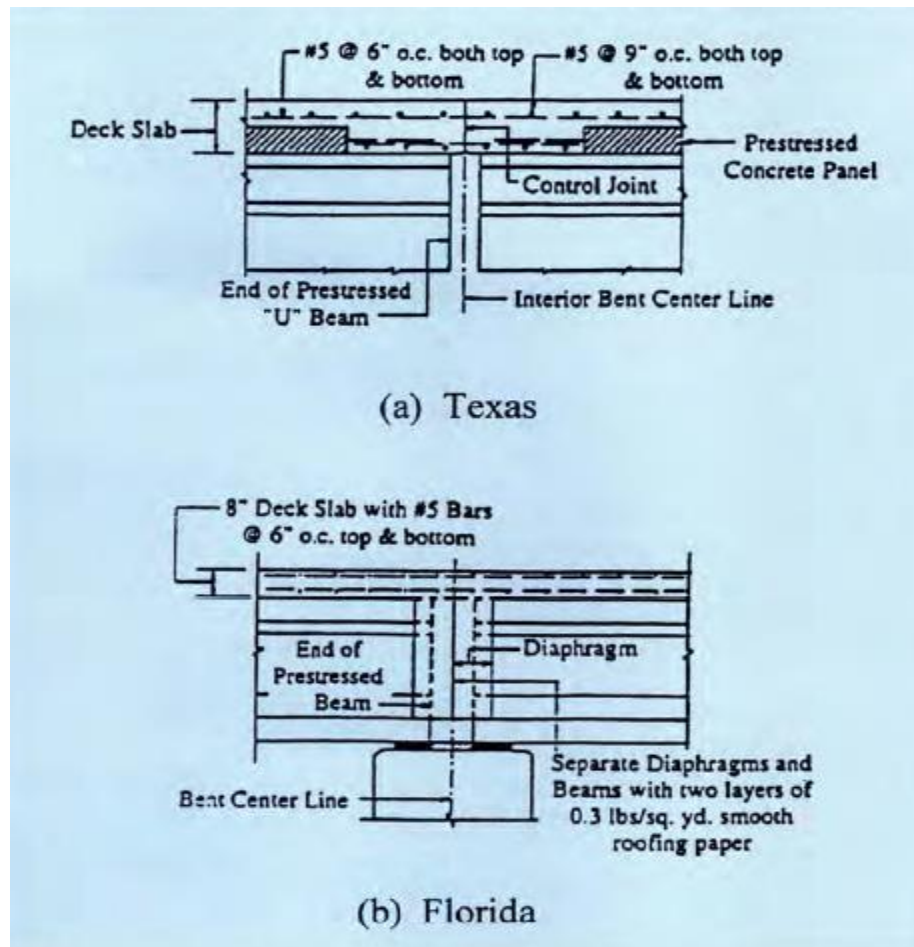
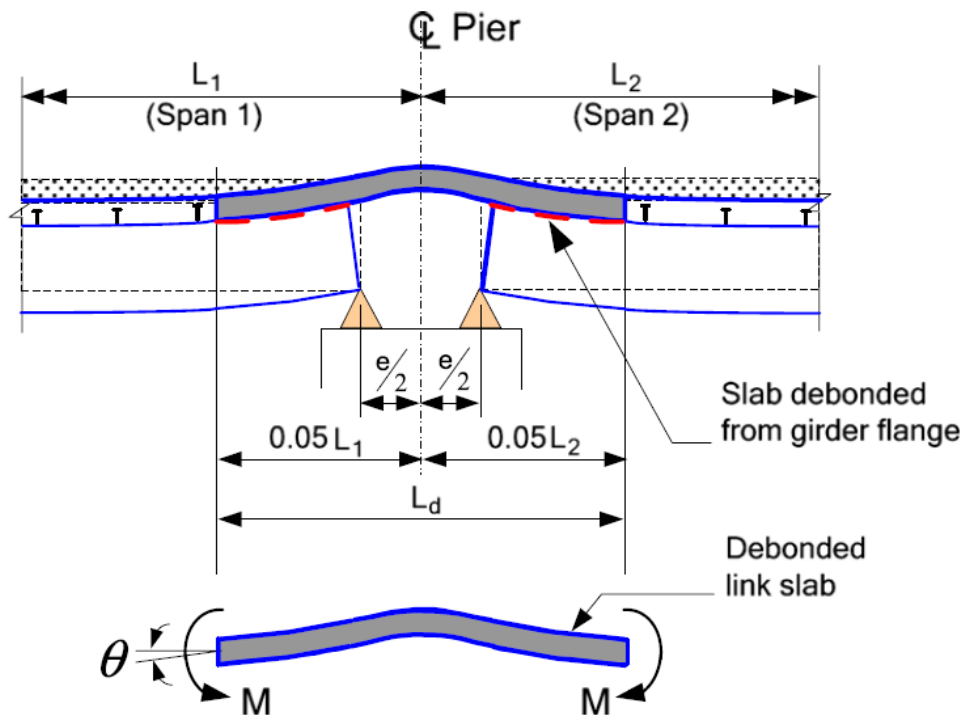


Figure 2.5: Typical jointless bridge configuration (Caner & Zia, 1998)

**2.2.2 Alexander Au, Clifford Lan, Jim Au and Bala Tharmmabala 2013**

The Ministry of Transportation of Ontario (MTO) conducted a research project on rehabilitation of multiple bridge decks with a debonded link slab system. To objective of this study was to acquire a better understanding on bridge rehabilitation using link slab. Also to assess the long-term reliability of this method, the MTO managed to accomplish this goal performed experiments with scale model to study the structural behavior of the link slab system and investigated a bridge rehabilitated using the debonded link slab system (Alexander Au, Clifford Lan, Jim Au and Bala Tharmmabala, 2013). A typical link slab configuration is illustrated in Figure 2.6.



**Figure 2.6: Debonded link slab system (Alexander Au, et al 2013)**

The MTO had revised the original design approach proposed by Dr. Caner and Dr. Zia (Caner and Zia, 1998). In the past, the design bending moment  $M$  caused by girder end rotations imposed on link slabs, were calculated in Equation 2.2:

$$E = \frac{2EI}{L_d} \theta \quad (2.2)$$

Where

$$E = \text{Young's modulus of concrete} \left( \frac{kN}{m^2} \right)$$

$$I = \text{second moment area of link slab section in concrete units} (m^4)$$

$$L_d = \text{total debonded slab length} (m)$$

$$\theta = \text{girder end rotation} (rad)$$

However, test results reflected that Equation 2.1 did not consider compatibility of the link slab and the girders, which could lead to unrealistic deformation in 3-D modeling (Au and Lam, 2011). Hence, the revised equation was proposed in Equation 2.3:

$$E = \frac{2EI}{L_d} \theta \alpha_R \quad (2.3)$$

Where  $\alpha_R$  is the adjustment factor to account for displacement between slab and girder within the debonded zone and given in Equation 2.4:

$$\alpha_R = \frac{4}{\left(1 + \frac{3e}{L_d}\right)} \quad (2.4)$$

Where  $e$  = distance measured from adjacent simple supports at the pier location in Figure 2.6.

The MTO conducted a series of lab tests to investigate structural behavior of the debonded link slab system. In addition, a finite element model was developed for comparison. The test specimens were subjected extensive cyclic loading in order to simulate the repetitive traffic loads on the bridge. The results showed that the cyclic loading pattern did not affect the overall stiffness of the link slab system because the slope of the load vs deflection curve remained constant. Likewise, strain in rebars were also not affected by the cyclic loading in the debonded link slab system. Crack patterns also indicated that the link slab was capable of carrying the load transferred by the girder end rotations by evenly distributed fine cracks along the width of the specimen. The crack pattern on link slab is shown in Figure 2.7. The experiment also validated that the 5% debonded zone between link slab and the supporting girder was sufficient.

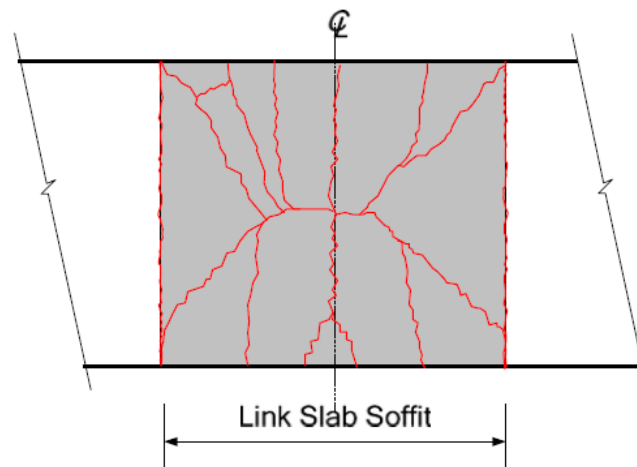


**Figure 2.7: Link slab crack pattern (Alexander Au, et al 2013)**

Furthermore, the MTO performed a field testing on a bridge that was previously rehabilitated with the debonded link slab system (Au and Lam, 2008; Au

et al. 2010). The structure was loaded before the installation of link slab to serve as the baseline. A total of 56 sensors were instrumented to collect structural response on selected locations. The bridge was loaded simultaneously by two trucks with weights of 441 kN and 430 kN. By comparing the theoretical and field test results, conclusions could be summarized as follows:

1. Although deflections and steel girder strains patterns in both approaches generally follow the same pattern, the predicted values by theoretical values were constantly greater than the records obtained in the field test.
2. Strains in steel girders showed the same pattern in both the theoretical model and field test results.
3. Field test data supported that the debonded link slab meet the SLS requirement of CHBDC 2000 and 2006. Thus, the proposed design methodology by Caner and Zia (1998) was validated.
4. The debonded link slab system provided minimum continuity to the bridge deck was successful in reducing girder end rotations, total vertical displacements and positive bending moments in the main span.
5. Equation 2.3 shown above was verified.

### **2.3.3 Kenneth M. Wing and Meryyn J. Kowalsky 2005**

The North Carolina Department of Transportation (NCDOT) carried out a research on bridge rehabilitation with the use of debonded link slab system (DLS). The west bound Plott Creek bridge on US highway 23-74 was selected to be

rehabilitated by the DLS. One of the most emphasizes of this project was to validate that the girders could be safely treated as simply-supported under service dead and live loads in the design of a debonded link slab system. A solar-powered sensor system was instrumented on selected locations to monitor the long-term response of the bridge. Meanwhile, theoretical values were calculated based on an analytical model.

Originally, the bridge had three interior expansion joints. Two of the expansion joints were eliminated during rehabilitation, except for the center expansion joint. Thus, two sets of link slab replaced the two expansion joints and one of which was monitored for its long-term performance. Based on design recommendation proposed by Caner and Zia (1998), the debonded link slab system was designed to accommodate a girder end rotation of 0.002 radians and the overall design followed the methodology by Caner and Zia (1998). The bridge configuration after rehabilitation is shown in Figure 2.8.

Sixteen thermocouples were installed to monitor temperatures on along the bridge. The devices were the FF-K-24 Omega thermocouples with a range of measurement up to 200 degree Celsius. In addition, 12 thermocouples were placed within the deck and four were installed on the steel girders. On each steel girder gauges were installed on both top and bottom.

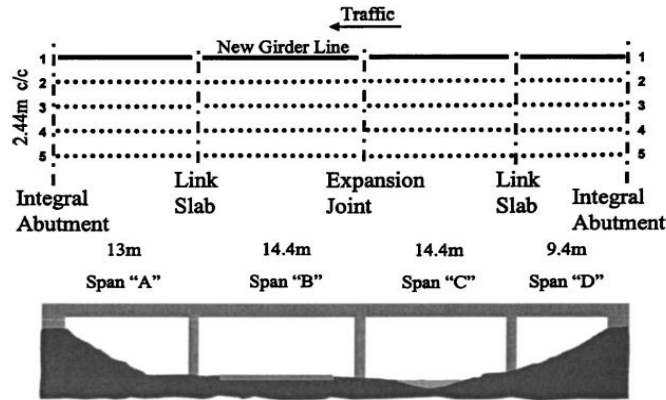


**Figure 2.8: NCDOT link slab rehabilitation design (Wing & Kowalsky, 2005)**

Live load tests were conducted in June of 2001, on two locations with four levels of applied loads. One of the locations was selected to produce the maximum positive moment in the span adjacent to the link slab. The other location was chosen to create the maximum negative moment in the link slab. On the other hand, the four load levels covered the normal service condition of the bridge: the first load was the weight of an empty truck, which was 137 kN; the third load has a magnitude of 304 kN, which represents the maximum allowable load for the specific truck without a permit; the second load level lied in the middle of the first and third load level, which in this case was 214 kN; the fourth load was 424 kN and is the maximum allowable load allowed on this bridge.

Based on the proposed configuration, a computer model was created to calculate end rotations of the steel girders. Because of the symmetry, only half of the spans were included where the other half was separated by a expansion joint and was not monitored by sensors. Each axle was modeled as a point load and one girder line was modeled at a time. The abutments were modeled as fixed supports and the

expansion joints were created as rollers. The link slabs were modeled as pinned connections at the girder end bearings. Comparisons of the results obtained from the live load test and the numerical simulation showed similarity in general, indicating that the girder demands could be sufficiently estimated by the load distribution formulas.

Long-term monitoring was fulfilled by recording the structural response of the bridge over the course of a year. The data were taken every two hours and lasted for two minutes. Approximately 40 readings were taken on each gauge. The bridge experienced a variation in temperature more than 15 degree Celsius daily. While the temperature could vary more than 45 degree Celsius seasonally. Results reflected that the thermal rotations measured were always smaller than the expected values due to large temperature fluctuation and momentary variations in surface temperature (Wing and Kowalsky, 2005).

Overall, results reflected that the debonded link slab system helped improve the bridge performance. The measured girder end rotations had never reached the design limit of 0.002 radians and the rotations recorded during the live load test were all smaller. Fine cracks were discovered on the link slab with a width of 1.6 mm, which was significantly smaller than that of a traditional expansion joint. Furthermore, the width of the fine cracks remained the same during the live load test, which was intended to simulate service condition of the bridge. This validated the serviceability of the DLS.

Furthermore, the authors also proposed a limit-state design method for link slab particularly on the bridge where the tests were conducted:

1. Calculate the negative moment caused by girder end rotations and cracking moment of the link slabs using Equation 2.5 and 2.6.

$$M_a = \frac{2E_c I_d \theta}{L} \quad (2.5)$$

$$M_{cr} = \frac{f_r I_d}{y} \quad (2.6)$$

where

$M_a$  = negative moment caused by girder end rotations

$I_d$  = moment of inertia of link slab

$\theta$  = girder end rotations

$L$  = length of link slab

$M_{cr}$  = link slab cracking moment

$f_r$  = flexural modulus of deck concrete

$E_c$  = elastic modulus of concrete

2. Compute stress in steel with Equation 2.7 (Caner and Zia, 1998).

$$f_s = \frac{f_r M_a}{6M_{cr} \rho \gamma^2 \left\{ 1 + \frac{\mu \rho}{3} - 0.333 [(\mu \rho)^2 + 2\mu \rho]^{0.5} \right\}} \quad (2.7)$$

where

$f_s$  = stress in reinforcing steel

$\rho$  = tension steel reinforcement ratio

$\mu = \text{modular ratio calculated as } \frac{E_s}{E_c}$

$\gamma = \text{distance to tension steel divided by overall section depth}$

3. Calculate the effective tension area of concrete in the main reinforcement by the Gergely-Lutz expression (McCormac, 1998) shown in Equation 2.8.

$$\omega = 0.076\beta f_s \sqrt[3]{d_c A} \quad (2.8)$$

where

$\omega = \text{estimated cracking width in units of } 0.003 \text{ mm}$

$\beta = \text{ratio of the distance to the neutral axis from the extreme tension fiber and from centroid of main reinforcement}$

$d_c = \text{concrete cover measured from extreme tension fiber to centroid of nearest reinforcement level in units of mm}$

$A = \text{effective tension area of concrete in the main reinforcing divided by the number of bars in } \text{mm}^2$

4. Calculate required reinforcement spacing by Equation 2.9 (Caner and Zia, 1998).

$$s = \frac{A}{2d_c} \quad (2.9)$$

5. Compute the number of bars by Equation 2.10.

$$N = \frac{b}{s} \quad (2.10)$$

where

*b = width of link slab in units of mm.*

6. Determine the area of reinforcement by Equation 2.11.

$$A_b = \frac{\rho b \gamma h}{N} \quad (2.11)$$

where

*h = overall section depth*

7. Eliminate results that are not feasible. Repeat the procedure until a satisfactory solution is achieved.

In conclusion, the study found that the controlling rotations on the link slab were not caused by traffic loads, but thermal. Hence, the design based on the assumption of simply-supported spans was adequate and conservative. Besides, it was identified that the link slab might have developed fine cracks during casting yet the effects on its performance is negligible. At last, the proposed design method can be used to develop a design chart and apply to specific applications of link slab.

# Chapter 3 Experiments

## 3.1 Objective and overview

To gain a better understanding on material properties of UHPC and ECC, a series of lab tests were conducted. The goal of the experiment was to obtain a hands-on experience on mix design; test material properties and compare the results with literatures; investigate sensor reliability, installation alternatives and propose recommended sensor designs for future experiment and bridge structural health/performance monitoring.

A total of 43 sensors were used on 14 specimens. The sensors are purchased from Resensys LLC<sup>TM</sup>, a company specializes in wireless structural health monitoring. Strain gauges used in the lab tests are also intended to be install on a bridge in future field tests. The experiment was intended to simulate the service loading pattern of link slab by applying cyclic loadings to the specimen. Experimental results and photos of each tested specimen were stored for result analysis in chapter 6.

## 3.2 Materials and expectations

### 3.2.1 UHPC

UHPC stands for ultra-high-performance concrete. UHPC is a cementitious concrete material that offers a minimum compressive strength of 120 MPa, or 17000 pounds per square inch, and a maximum compressive strength of 200 MPa, or 29000 pounds per square inch (psi). Fibers serve as reinforcement in material in order to

satisfy specific requirements of strength, durability, ductility and toughness depending on applications. Conventional fibers including PVA, Glass or high carbon steel. UHPC materials can provide much better ductile behavior compared to normal concrete. 3 out of the 14 specimens were casted as UHPC material.

### **3.2.2 ECC**

Engineered Cementitious Composites, also known as ECC, represent a group of ultra-ductile fiber reinforced concrete (Li, 2011). Usage of ECC materials are not limited in laboratory. They are also used in large-scale on-site construction projects (Kong et al, 2003; Lepech and Li, 2007). Characteristics of ECC material includes high tensile strength and ductility. Another typical application of the material is structural repair. In addition, ECC material offers environmental benefit with negative carbon footprint. The material provides much higher resistance against weather by developing fine cracks. 11 out of the 14 specimens were made as ECC materials.

### **3.2.3 Expectation**

Expectations of experimental results were made based on material properties discussed in previous sections. First, a high tensile strength was expected for both materials. The high tensile strength is one of the most essential benefits offer by UHPC and ECC for reduction in reinforcement and member size. Another critical property is the high tensile ductility of the material. Hence, it was expected that the material would display a “yield point” similar to that of a steel and experienced “metal-like” deformation with large curvature. Also, tendency of fine crack development allows the material to protect the rebars and substructure from chloride-

contaminated water infiltration and debris accumulations. So that fine cracks were expected to be observed along the width of the specimen. And a fracture plane formed by multiple fine cracks is also expected to appear when the specimen failed.

### **3.3 Testing**

#### **3.3.1 Sensor information**

Sensors used in this experiment were the Strain Gauge SenSpot™ Sensor.

Each sensor consist of a strain gauge that serves as a strain sensing element; a cable and a wireless transmitter delivering data to monitoring programs. The Strain Gauge SenSpot™ Sensor is shown in Figure 3.4 and 3.5. This product had been used in industry for real-time and long-term structural health monitoring. The sensor allows data to be taken wirelessly and has several features making it suitable for this test because the same type of sensors is planned to be install on a bridge in future field test. First, the Strain Gauge SenSpot™ Sensor is designed to be durable, with a minimum battery life for 10 years and the sensor needs no or minimum maintenance. The size of the sensor is small with dimensions of 2in. x 2in. x 1in. and weighs only 50oz, communicating at IEEE 802.15.4, 2.4GHz. The small size, combing with the self-adhesive or flange mount, allows the sensor to be easily installed on test locations. The working temperature of the sensor is -40 to 150 degree Fahrenheit ( -40 to 60 degree Celsius) and this range covers the temperature variation of both the experiment and field test.



**Figure 3.1: Strain Gauge SenSpot™ Sensor**



**Figure 3.2: Sensor installation on a bridge girder**

### **3.3.2 Sensor installation**

The sensors were designed to be placed on specimen made of ECC and UHPC to study their behavior under cyclic loading. Whereas, one of the challenges in this experiment is to simulate actual working condition in the lab test for the sensors as if they were working on structural members in a real bridge. Hence, modification was made during sensor installation in order to simulate field condition of the sensors. There were two types of sensor systems designed. Originally, the sensor is designed

to be directly install on a structural member by self-adhesive or flange mount. This was chosen to be the first approach of sensor placement, which translated into directly installation of sensors on the surface of the concrete specimen. Another option was to mount the strain gauge of a small piece of steel plate, forming a sensor system. Then this sensor system was installed on the surface of the concrete specimen in the same manner as the first alternative. The only difference was the steel plate being the intermediate material between the strain gauge and the concrete. Ideally, the two types of sensors should return similar results when placed within the same region. If not, relationship between them can be studied.

However, this method of installation could raise concerns over accuracy of data acquisition by introducing potential sources of uncertainties. Unlike field condition, where the sensor is installed directly on a structural member, the strain gauges here were install on a metal plate. Technically, the strain gauges were measuring strains on the metal plate, instead of the concrete specimen. Thus, it was assumed that the metal plate remains compatible with the ECC and UHPC specimen. In addition, it was also assumed that the bonding between the metal plate and the strain gauge remain strong enough for the sensor to capture any displacement. To eliminate discrepancy, calibration was performed during data analysis for each sensor because the metal plate might develop strains before the test began. For instance, if the data showed  $150\mu\epsilon$  at time 0, the entire data set would be deducted by  $150\mu\epsilon$ .

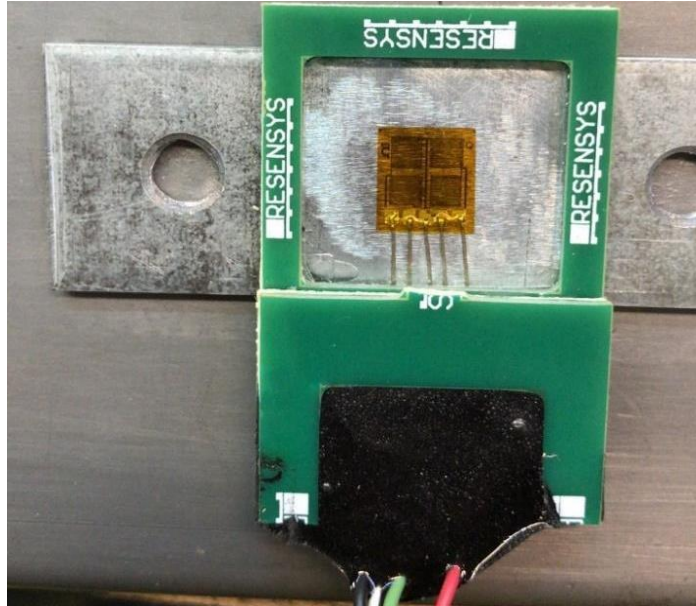


**Figure 3.3: Strain gauge installation on a metal plate**

### **3.3.3 Procedure**

Fourteen link slab specimens were casted in the NRMCA's International Center for Concrete Research. When ready, all specimens were tested by three-point bending test and the procedure followed ASTM C78/C78M-18. Schematic of the testing apparatus is shown in Figure 3.4. During mixing, ECC materials were modified for the purpose of the testing. The updated mixture is presented in Table 3.2. There were 43 strain gauges on 14 specimens. To simulate field condition, the strain gauges were installed on a small metal plate prior to mixing. The sensor distribution is summarized in Table 3.1. Note that "bdi" and "hbm" are two types of sensors that were also tested here. With the sensor system established, some of the sensors were buried during pouring of the concrete specimen and others were installed on surface of the specimens. A picture of the finished product is presented in

Figure 3.5. Each specimen was loaded until failure. In order to simulate service condition on bridge for the link slabs, loads were applied cyclically, where on average each specimen had 5 loading cycles until it reached its failure point. During testing, data of applied loads and corresponding stresses were recorded continuously. However, the data was discretized at a one-second interval for data processing. Strains of the specimens were also monitored throughout the testing, where the readings were taken every 0.2 seconds on average. Similarly, strain data were converted into the same time interval of the stress data in data analysis.

**Table 3.1: Sensor distributions**

Test No.	Material	No. of Sensors	Sensor Locations
1	UHPC	4	Top Concrete, Bottom Concrete, Top Steel, Bottom Steel
2	UHPC	4	Top Concrete, Bottom Concrete, Top Steel, Bottom Steel
3	ECC	4	Top Concrete, Bottom Concrete, Top Steel, Bottom Steel
4	ECC	4	Top Concrete, Bottom Concrete, Top Steel, Bottom Steel
5	ECC	1	Embedded Bottom Steel
6	ECC	1	Embedded Bottom Steel
7	ECC	4	Top Concrete, Bottom Concrete, Top Steel, Bottom Steel
8	ECC	2	Top Concrete, Top Steel
9	ECC	3	Bottom bdi, Bottom hbm, Bottom Concrete
10	ECC	2	Bottom bdi, Bottom Concrete
11	ECC	4	Bottom bdi, Bottom Steel, Bottom Concrete, Bottom hbm
12	ECC	2	Bottom Concrete, Embedded Bottom Steel
13	ECC	4	Bottom Concrete, Bottom bdi, Bottom hbm, Embed Steel
14	UHPC	4	Top Concrete, Bottom Concrete, Top Steel, Bottom Steel

Note that the 3 UHPC specimens were casted strictly based on specifications from the manufacture. On the contrary, there were more flexibility when designing the ECC specimens. Hence, the ECC specimens provide an opportunity to explore different mix design by trail and errors. As a result, ECC became the focus in material

testing. The final mix design for ECC was shown in Table 3.2. The selected design was chosen based on the similarity to the mix design (Li, 2008) recommended in Section 3.1 in order to achieve the desired high tensile strength and ductility.

**Table 3.2: Updated ECC mixture**

Material	By weight
Cement	1
Fly ash (Class F)	1.2
Silica Sand (20-30 or finer)	0.8
Water	0.53
HRWR (Types A&F)	0.013
PVA Fiber	2% (by volume)

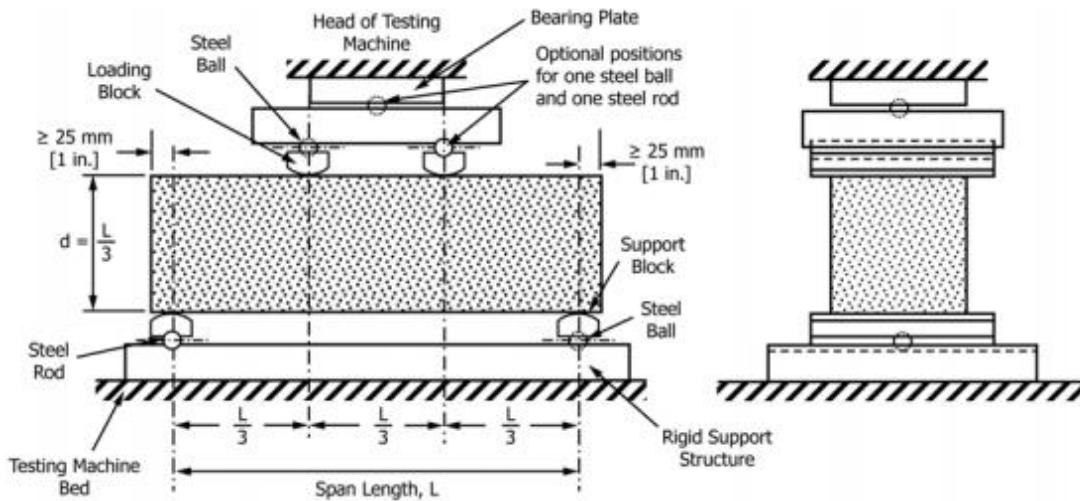


**Figure 3.4: Three-point bending test apparatus (ASTM C78/C78M-18)**



**Figure 3.5: Link slab specimen with strain gauge**

It is worth pointing out that the SenSpot™ sensor is generally applied on steel members as shown in Figure 3.2. Hence, practicality of the sensor on concrete material remains unclear. Experiments in this section would not only carry out results on material properties of ECC and UHPC, but also provide insights on performance of the SenSpot™ sensor on concrete materials. This is of great value as the tests offered potential on expanding the use of this type of sensor on materials other than steel.

Practicality of the SenSpot™ sensor in this project is secured by the characteristics of ECC and UHPC. In fact, both ECC and UHPC tend to develop fine cracks that are hairline in width, so that disturbance due to crack development is not significant. Nevertheless, discrepancies were found in data analysis, reflecting that the sensors were only reliable within a certain range of measurement. This subject will be discussed in chapter 6.

## Chapter 4 Finite Element Analysis

### 4.1 Description

Numerical analysis was done to simulate the bridge behavior under service condition. The goal of numerical simulations is to obtain a preliminary assessment of structural performance of the bridge under service condition. In this section, 2 models were generated based on finite element methods. Computer programs Ansys Workbench<sup>®</sup> and CSiBridge<sup>®</sup> were utilized to create finite element models and the results were compared. The purpose of this section is to create a baseline for future installation on link slabs and corresponding numerical simulations.

In fact, models developed for numerical simulation were created as a prototype structure. Namely, the models were only going to include the concrete slabs and steel girders underneath. All other components in the substructures, such as bents and abutments were not directly included in the model. Also, the reinforcing rebars were also excluded. Instead, substructures were translated into boundary conditions and bearings to simulate their presence and the competence of the bridge model was ensured mechanically. However, some of the attributes in dynamics response, for instance, the mass matrix, were changed by simplifying the bridge model. Hence, when results from numerical simulation and field test were compared, it was anticipated that they might not perfectly reflect each other. Nevertheless, as long as the results fall into the acceptable range, it was considered reasonable for the purpose of this thesis.

## 4.2 Bridge Details

The bridge serves as an overpass bridge on Winch Road, crossing interstate highway 95 in the Maryland state highway system. The structure number is CEX952001 and it was designed as a composite bridge with steel girders and concrete slabs. The length of the bridge is 215.5 feet and it is 31.17 feet wide. There are 4 spans and the reinforced concrete decks are 2 inches apart. The gap between the concrete decks are designed to be filled by expansion joints. The expansion joints are considered as non-structural component. Therefore, the joints were eliminated in the finite element analysis in later sections. The expansion joints are to be replaced by link slabs in the future. As previously discussed, all 4 reinforced concrete decks are supported by steel girders below, where the exterior girders are W36x135 and the interior ones are W27x94. Each girder has the same length as the concrete decking it supports. Unlike the gap between decks, bearings supporting the steel girders are 8 inches apart measured from center to center. The bridge is designed as a simply supported bridge with constraints only on translational motions. The bridge is free on rotation. Specifically, bearings located at the center and two ends restrict translations in all x, y and z directions. While other 2 sets of bearings only prevent motions in z (vertical) direction. Photos of the bridge and some of its structural drawings are shown in Figure 4.1 to 4.2.



**Figure 4.1: Plan view of bridge CEX952001**



**Figure 4.2: Elevation view of bridge CEX952001**

## 4.3 Finite Element Model using ANSYS Workbench®

### 4.3.1 Overview

According to information discussed above, a finite element model was created in Ansys Workbench® to simulate behavior of the bridge under service condition. Results of interested are the bridge responses to moving truck loads and its modal frequencies. The model generated by Ansys Workbench® only carried out the results of the first six modal frequencies and corresponding modal shapes, while the model created in CSiBridge® would include both the structural response of standard moving truck loads and modal analysis. An overview of the model by Ansys Workbench® is presented in Figures 4.3 to 4.4.

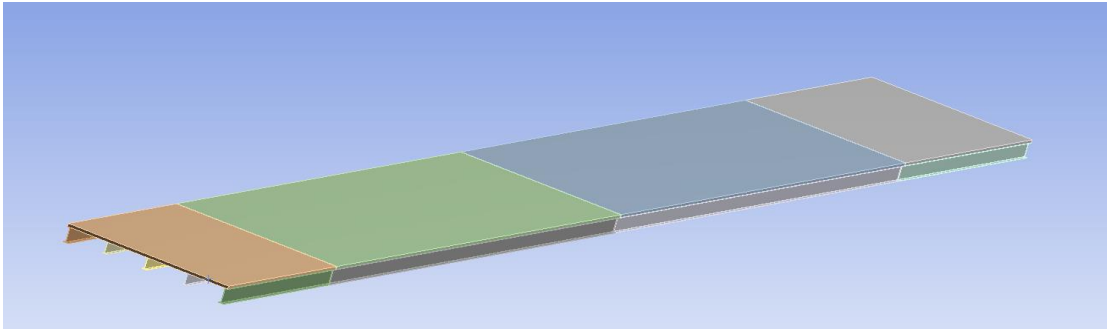


Figure 4.3: Bridge model geometry in Ansys Workbench®

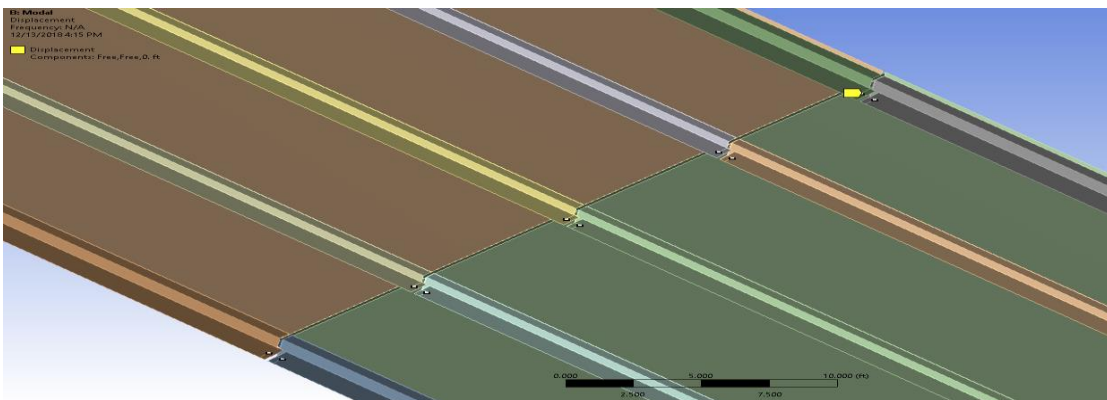


Figure 4.4: Boundary conditions at bearings

### **4.3.2 Results for Modal Analysis**

The results for the first 3 modal frequencies and corresponding modal shapes are shown in Table 4.1 and Figure 4.5 to 4.6. In fact, meshing elements were program-controlled in this Ansys Workbench<sup>®</sup> model. There were 3 primary element types used in this analysis: Tet10, Hex20 and Wed15 per Ansys Workbench<sup>®</sup> documentation. Specifically, Tet10 represents a 10-node linear tetrahedron element with 3 degree of freedom at each node, which is used to model irregular shapes. On the other hand, Hex 20 is a 20 nodes linear hexahedron that also has 3 degrees of freedom for each node. Hex20 is normally used for quadratic displacement behavior. At last, Wed15 is defined as a 15-nodes linear wedge (prism), with 3 degree of freedom and used for quadratic displacement behavior. Application of each element was controlled by Ansys Design Modeler<sup>®</sup> to specific conditions where a particular mesh was generated. Visualizations of the 3 primary meshing elements can be viewed in Figure 4.5.

**Table 4.1: Modal frequencies by Ansys Workbench<sup>®</sup>**

Modes	Frequency (Hz)
1	2.5307
2	2.7159
3	3.0581
4	3.3124
5	5.8249
6	6.1092

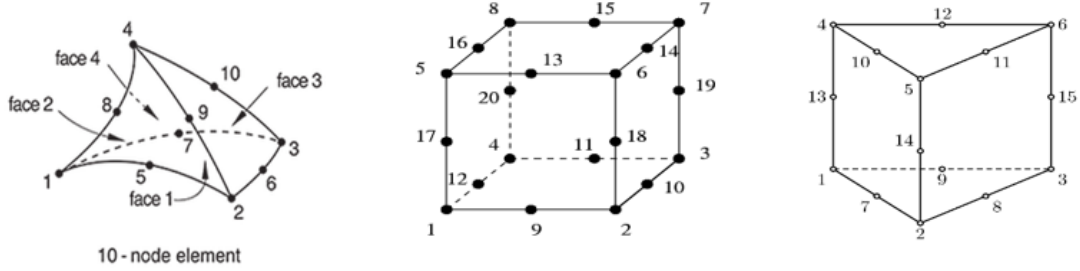


**Figure 4.5: Tet10, Hex20 and Wed15 elements in Ansys Workbench®**

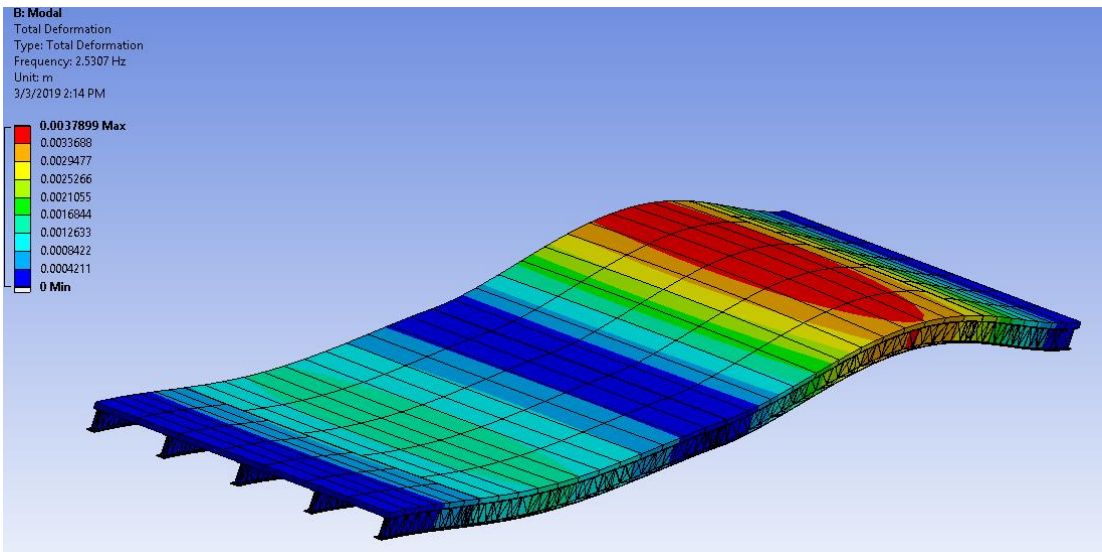


**Figure 4.6: Total deformation in dynamic analysis**

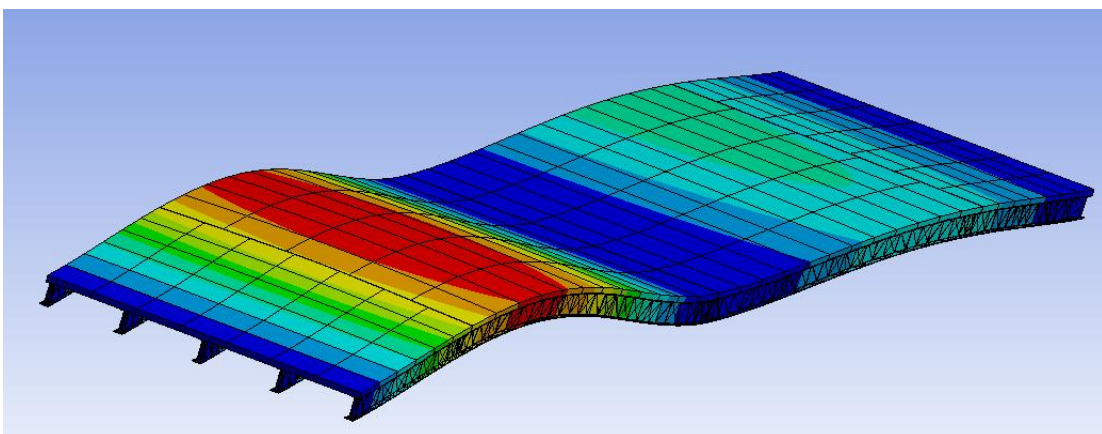


**Figure 4.7: 1st modal shape,  $f = 2.53$  Hz**

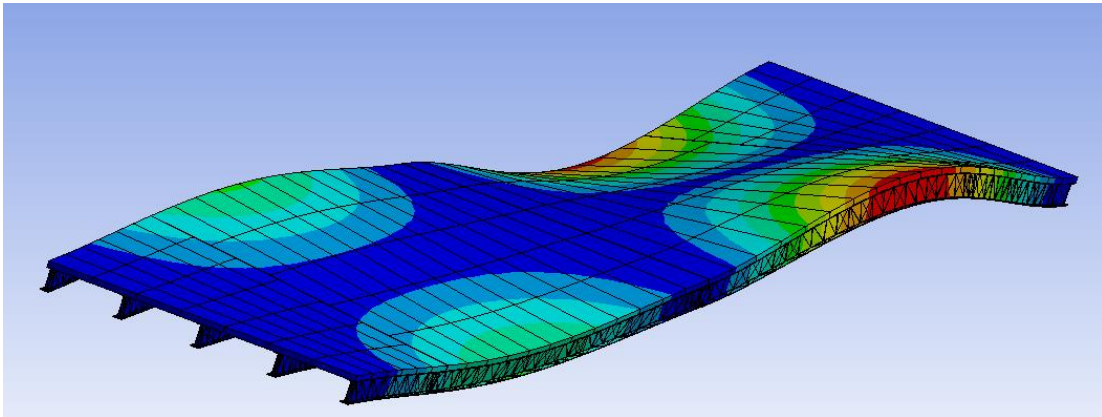


**Figure 4.8: 2nd modal shape,  $f = 2.72$  Hz**

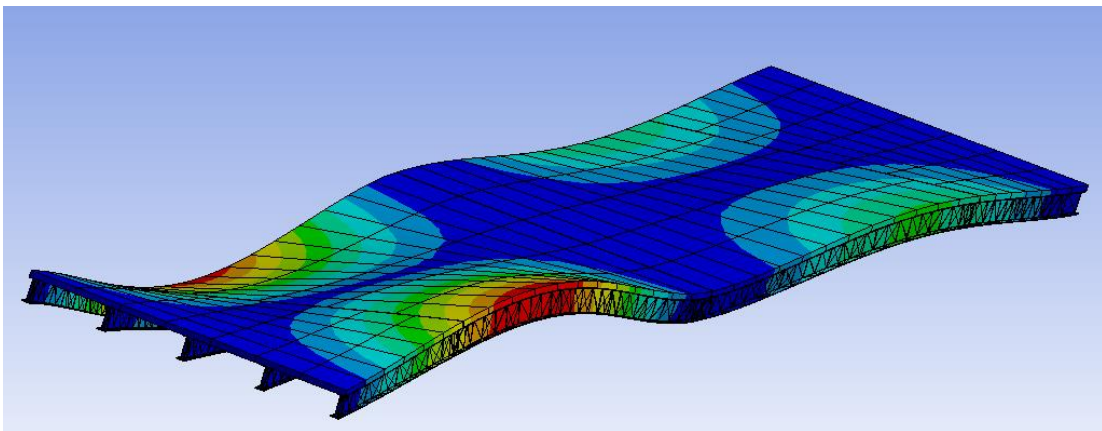


**Figure 4.9: 3rd modal shape,  $f = 3.58$  Hz**

## **4.4 Finite Element Model using CSiBridge<sup>®</sup>**

### **4.4.1 Overview**

Based on the same bridge layout, a finite element model was generated using CSiBridge<sup>®</sup>, which is a more production-oriented software. The bridge was modeled as simply-supported at bearings. The model consist of three spans with a skew angle of 6.4 degrees. There were three types of restraints: fixed bearings resist translational

motions in x, y and z directions; joint bearings resist translational motions in y and z directions; deck restraints resist translational motions in y and z directions to prevent the structure from moving sideways in modal analysis.

#### **4.4.2 Shell Elements vs. Solid Elements**

Unlike the model in Ansys Workbench<sup>®</sup>, where the bridge was modeled using solids, the structure was modeled using shell elements in CSiBridge<sup>®</sup>. In general, shells are considered as a mathematical simplification of solids. Shell elements are limited to objects that are thin, meaning that the thickness of the body should be approximately 20 times less than the span. This makes the shell elements applicable to this bridge model because the structure has a span of 215.5 feet, while the thickness only consist of the thickness of the slab and the depth of the supporting girders.

Shell elements boost the computation process by allowing fewer elements when modeling thin objects. Additionally, shell elements make meshing easier and are less prone to negative Jacobian errors that could take place in extremely thin solid elements. An overview of the model using CSiBridge<sup>®</sup> is shown in Figure 4.10.

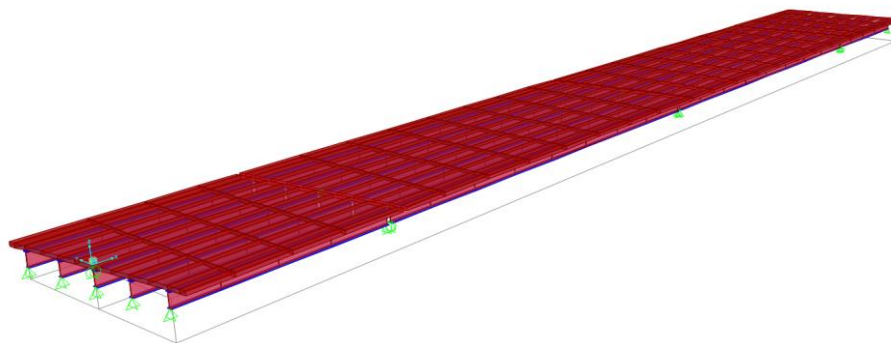


**Figure 4.10: CSiBridge<sup>®</sup> model using shell elements**

### **4.4.3 Results for Modal Analysis**

The first six modal frequencies of the bridge model are summarized in Table 4.2 and the first three modal shapes are presented in Figures 4.11 to 4.13.

**Table 4.2: Modal frequencies by CSiBridge®**

Modes	Frequency (Hz)
1	2.4636
2	2.6572
3	3.6629
4	3.8235
5	7.5090
6	7.8355

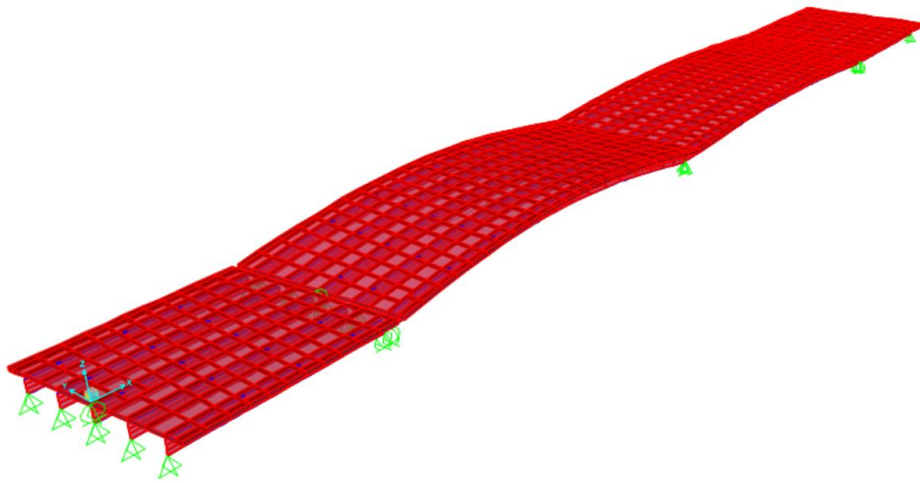


**Figure 4.11: 1st mode shape,  $f = 2.46$  Hz**

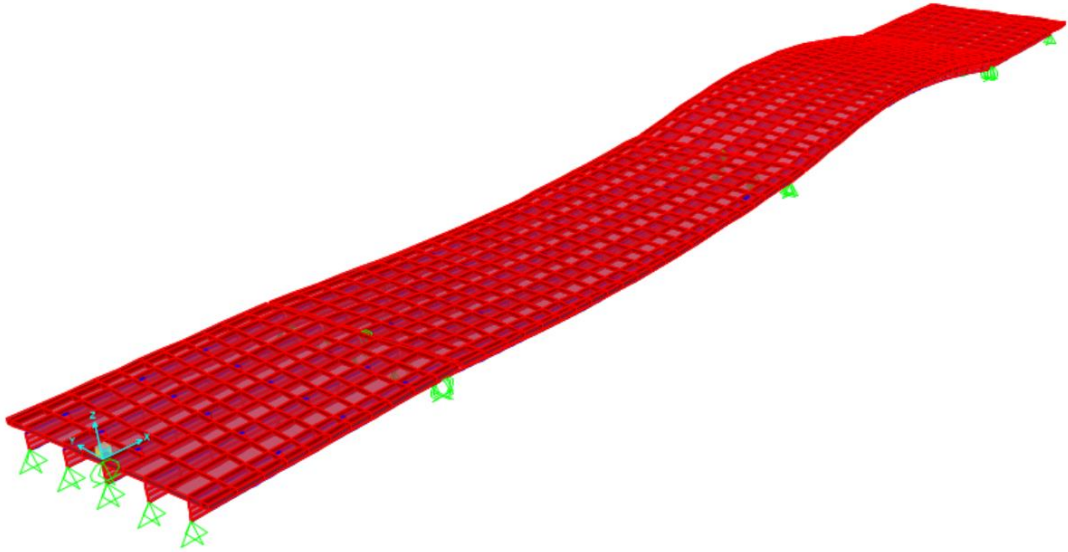


**Figure 4.12: 2nd mode shape,  $f = 2.65$  Hz**

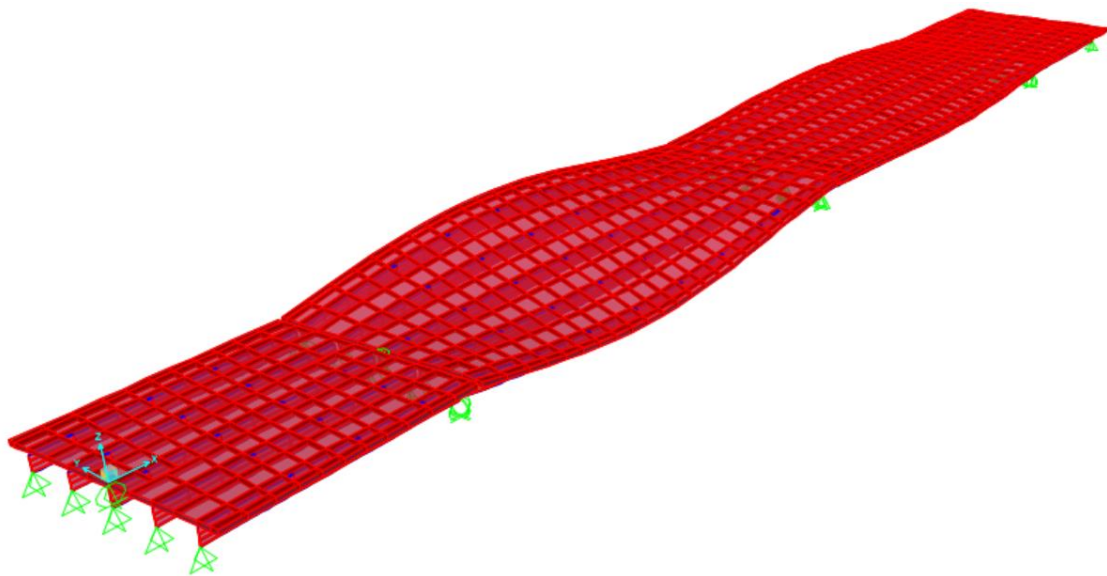


**Figure 4.12: 3rd mode shape,  $f = 3.66$  Hz**

#### 4.4.4 Structural Response for Moving Truck Loads

Standard moving truck loads were applied to the bridge and the structural responses were simulated. The vehicle load was chosen as HSn-44 per AASHTO specifications, which stands for truck with a semi-trailer. The truck load consists of vertical applied forces from three axles of the vehicle. An example of a HSn-44 vehicle load is shown in Figure 4.13. The model included two standard trucks moving at 40 MPH in opposite directions. Figure 4.14 demonstrates the moving truck situation. The duration of the simulation was set to 200 seconds and the applied loads were discretized every five seconds. In other words, the simulation lasted for 200 seconds and each frame was shown every five seconds. To gain a better visualization of the structural response, magnification factor was set to 50.

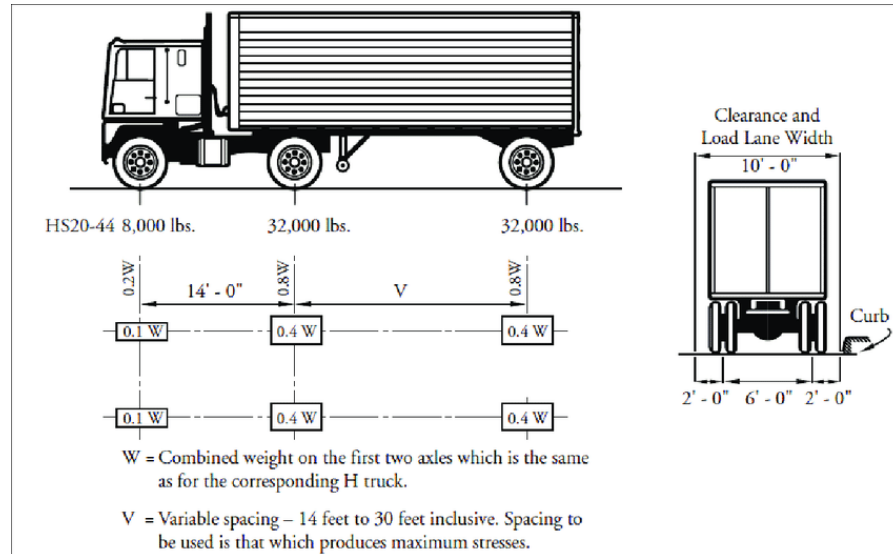


**Figure 4.13: HS20-44 vehicle load per AASHTO specifications**

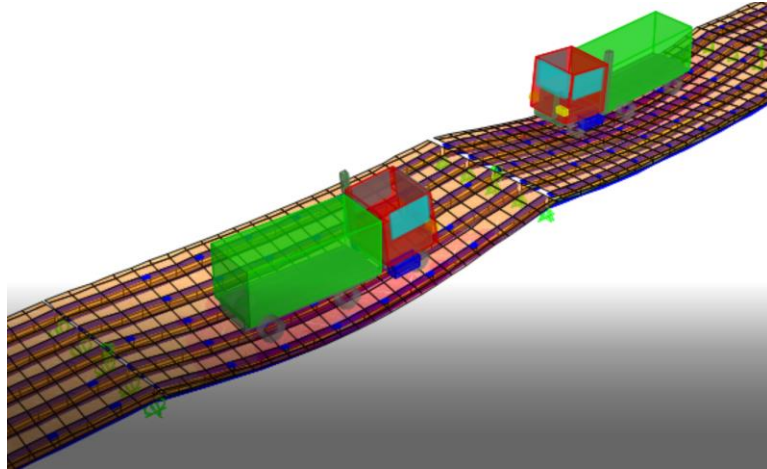


**Figure 4.14: Moving truck loads visualization**

The maximum positive and negative vertical shear forces were plotted in Figure 4.15, with a maximum positive shear force is 62.5 kips and the maximum negative shear force is -59.4 kips. The maximum positive shear force is recorded at 109 feet from the initial station and the maximum negative shear force occurs at 34 feet from the initial station. The figure was plotted along the length of the bridge and the positive values indicate shear forces in the positive z direction; while the negative values represent shear forces in the negative z direction.

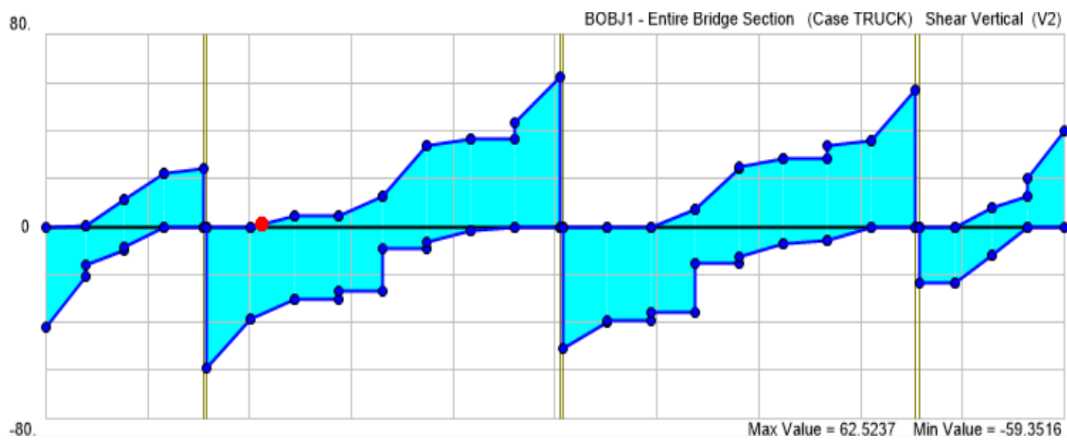


**Figure 4.15: Maximum and minimum vertical shear envelop**

Moments about the horizontal axis (x-axis) is plotted in Figure 4.16. The maximum positive moment is 1036.41 kip-ft and the maximum negative moment is 46.92 kip-ft. The maximum positive moment occurs at 147 feet from initial station of the bridge and the maximum negative moment occurs at 184.5 feet measured from the initial station.

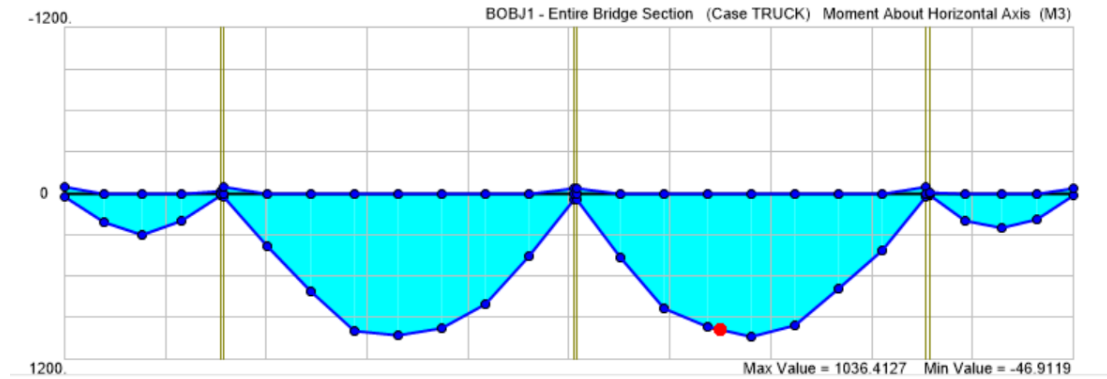


**Figure 4.16: Maximum moment envelop**

Vertical displacements/deflections over the entire section is shown in Figure 4.17. Since there are no displacements in the upwards direction, all the values are negative. The maximum displacement is 0.88 inches in the negative z direction; the minimum displacement is 0.0003 inches pointing downwards. The maximum deflection occurs at 147 feet measured from the initial station and the minimum deflection occurs at 185.2 feet from the initial station.

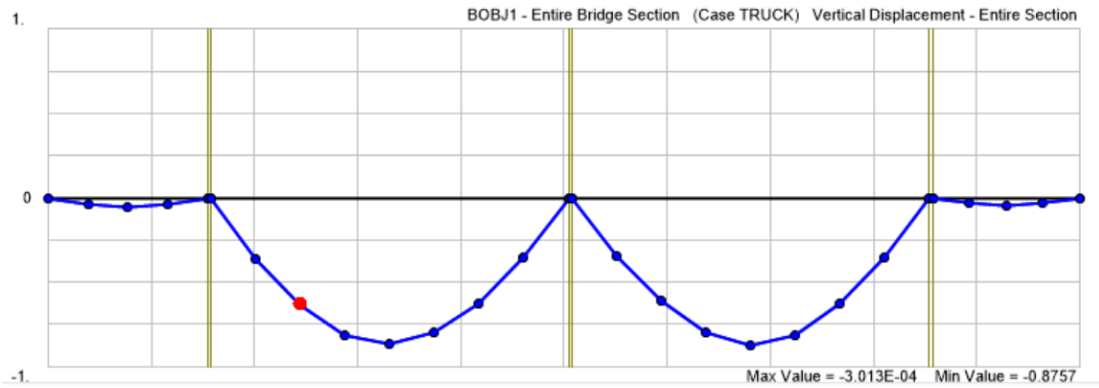


**Figure 4.17: Maximum vertical deflection**

## 4.6 Modal Analysis Comparison

Modal frequencies from the two models were summarized in Table 4.3. It can be inferred that the two models generally agree with each other, with minor differences. Results for the first two modes were close, while the difference between the two models increases in higher modes and the average error was calculated as 16.2%. The model generated by the CSiBridge<sup>®</sup> is expected to be more accurate. However, results in the numerical simulations need to be examined by data collected in the future field test for validation.

**Table 4.3: Modal analysis comparison**

Modes	Frequency by Ansys Workbench <sup>®</sup> (Hz)	Frequency by CSiBridge <sup>®</sup> (Hz)	Error (%)
1	2.5307	2.4636	2.7
2	2.7159	2.6572	2.2
3	3.0581	3.6629	19.8
4	3.3124	3.8235	15.4
5	5.8249	7.509	28.9
6	6.1092	7.8355	28.3

# Chapter 5 Field Test

## 5.1 Description

### 5.1.1 Strain Distribution

Field tests were scheduled to validate performance of link slab. Specifically, strain distribution and crack propagation will be closely monitored. In principle, design of link slab is strain-controlled. The depth of concrete and rebar placements are determined based on limit states in strain. Ideally, the strain distribution is assumed to vary linearly, similar to the strain diagram of a Whitney's stress block. Hence, the maximum strain values will occur at the top and bottom location, representing the extreme compressive and tensile fibers. Figure 5.1 illustrates the strain distribution of ECC and UHPC link slab by design.

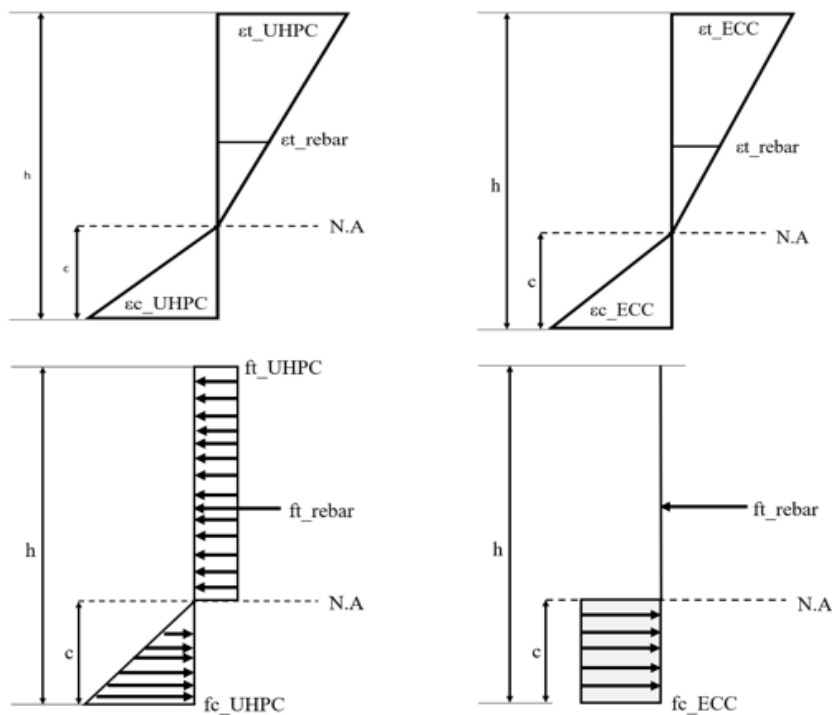


**Figure 5.1: Strain distribution of link slab**

### **5.1.2 Sensor System Configuration**

Ideally, fine cracks are expected to be formed when the link slab is subjected to bending moment imposed by girder end-rotations. Therefore, it is considered a failure if concentrative, visible, major cracks occur on the link slab. Another limitation during design is associated with sensor placement. The sensors need to be mounted on a small piece of metal plate in order to be stabilized on designated locations. Hence, the strain gauge will not be measuring the movement of the concrete link slab directly. Instead, the readings rely on compatibility between the link slab and the metal plate. During data analysis, feasible range of measurement and sensor calibration need to be done. Information on this subject will be discussed in Chapter 6.

## **5.2 Preparation**

Sensors are to be placed on girders in both top and bottom location to measure strains of the ECC and UHPC link slabs. The adjacent girders will both be instrumented with strain gauges symmetrically. The layout is shown in Figure 5.2 as an elevation view. For two adjacent girders, there will be 4 sensor systems and 2 on each girder. On each link slab, only one sensor will be activated for data acquisition and the other one will serve as a redundancy in case one of the sensors is damaged. Figure 5.3 and 5.4 are the elevation views of the sensor locations.

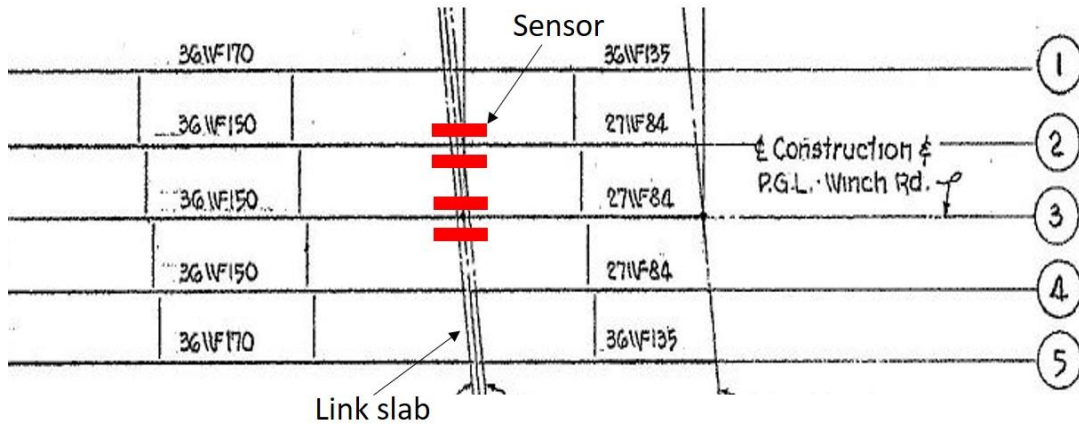


**Figure 5.2: Plan view of sensor locations**

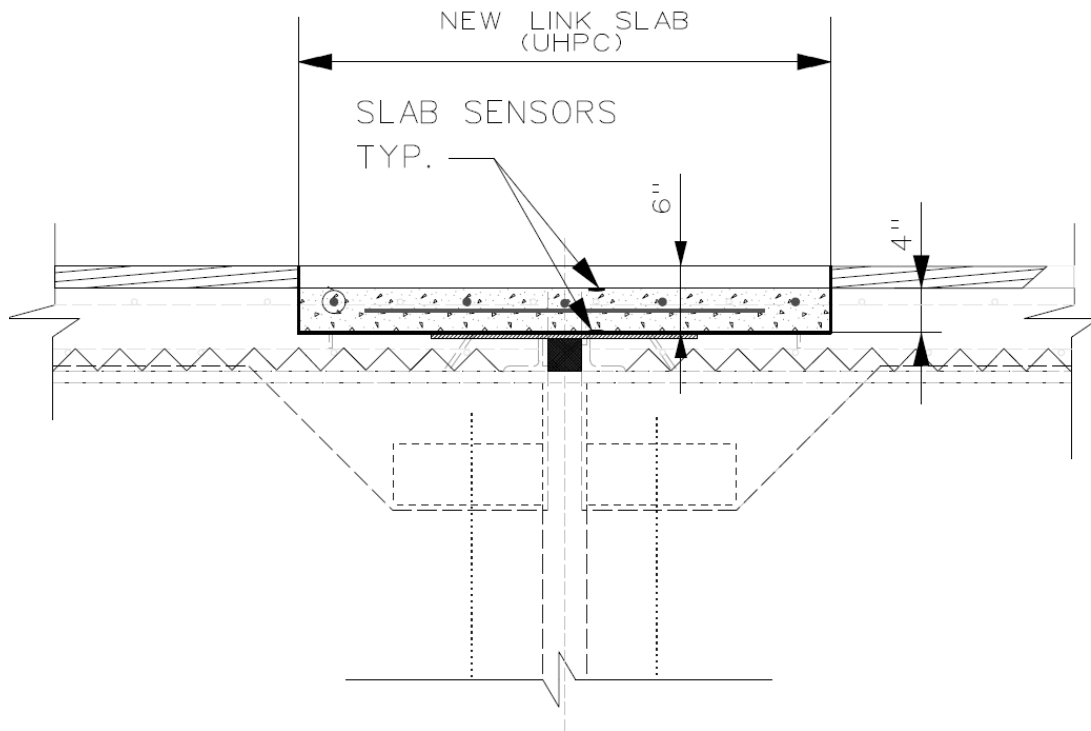


**Figure 5.3: Elevation view of sensor location on UHPC link slab**

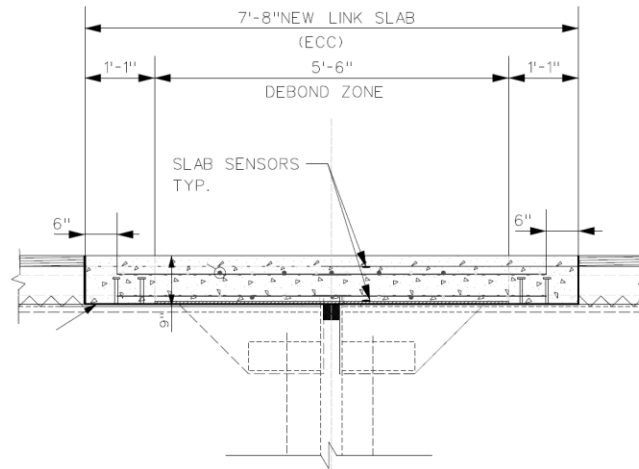


**Figure 5.4: Elevation view of sensor location on ECC link slab**

### 5.3 Equipment

Unlike shown in chapter 3, where there are two types of sensor systems in the lab tests, the field test is only going to use the sensor configuration shown in Figure 5.5. In this set-up, a single strain gauge is mounted on a piece of steel plate and connected to a transmitter with wires. The transmitter will be mounted on the outside surface of the bridge parapet. When the sensor system established on the bridge, real-time data are to be collected by the data acquisition (DAQ) system located in a area with limited access 50 to 150 feet away from the transmitter. Data will be transported wirelessly. Then, the DAQ will deliver the data to a remote server using commercial cellular service. The long-term monitoring of the performance of the link slab will be conducted as discribed above. Figure 5.6 shows a DAQ equipment and Figure 5.7 is a simple representation of the network for data collection.

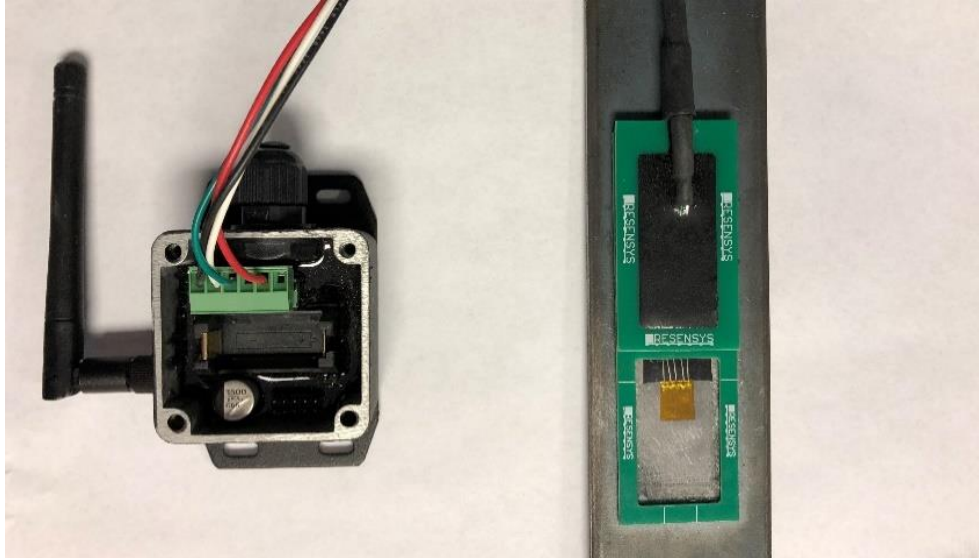


**Figure 5.5: Sensor system with a steel plate**



**Figure 5.6: Solar powered DAQ**

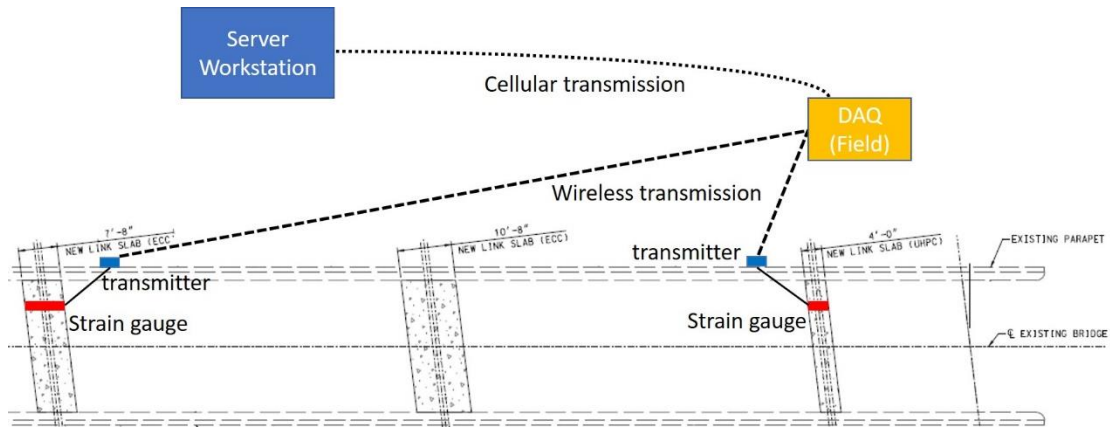


**Figure 5.7: Network of data collection**

## 5.4 Procedure

The entire operation includes two parts: existing joints remove and construction of the link slabs. Procedures for ECC and UHPC link slabs are slightly different: for link slabs made of ECC, bottom sensors will be placed on the roofing paper above girders after removal of existing joints and decks; while for UHPC link slabs, existing joints will be removed completely but the deck will be partially removed and bottom sensors will be installed on sealing between the gap. During concrete pouring, the top sensors are to be placed on top of the deck and covered by overlay concrete. Cables of the sensor systems are fixed along the link slab and extended outside. When the concrete has cured, the cables will be connected to the transmitters to initiate the long-term monitoring process of the project.

## **Chapter 6 Results**

### **6.1 Results for ECC and UHPC**

#### **6.1.1 Data Processing**

Fourteen tests were conducted in the NRMCA's International Center for Concrete Research, including three UHPC specimens and 11 ECC specimens. Each specimen was loaded with cyclic loading until failure. During testing, fine cracks developed on the link slab specimen and a major crack marked the failure state of the specimen. It is possible to have fine cracks when the specimen was being casted, but it is acceptable for link slab.

Each test lasted approximately an hour on average, where readings for applied loads and stresses were taken every five seconds. On the other hand, strain data were recorded every 0.2 seconds on average. Hence, in order to generate the stress-strain curve, the strain data were discretized and converted to one data point for every five seconds, to match the frequency of the stress data. In addition, desyncs were noticed in data collection. That is, there were time lags between the stress and strain data because they were not necessarily recorded at a same time. The stress data could be recorded long after the strain data because the strain gauges started to take readings as soon as they were installed on the specimen. In data processing, this scenario was adjusted by carefully shifting the two data so that both readings would start at a same time, where the first load was applied. Additionally, random errors in readings were identified and outliers were manually removed from the data sheet.

### **6.1.2 Maximum compressive strength**

Table 6.1 summarizes the maximum compressive strength of the specimens. Note that compressive strengths for the three UHPC specimens were not recorded due to its ultra-high compressive strength so its compressive strength is generally not a concern, when compared to its tensile behavior. In fact, the three UHPC specimens were casted strictly followed by the mix design provided by the manufacturer LafargeHolcim™. Based on specifications provided by the manufacturer, the maximum compressive strength of the UHPC specimens is 14000psi. Unlike UHPC, ECC specimens were casted based on a mix design shown in table 3.1, which was determined by trial and error. Consequently, there was more flexibility in ECC because it was possible to select or modify the mix design to investigate how the optimal solution could be achieved.

**Table 6.1: Maximum compressive strength**

Test No.	Material	Compression strength (psi)
1	UHPC	N/A
2	UHPC	N/A
3	ECC	9497
4	ECC	9497
5	ECC	11597.8
6	ECC	11597.8
7	ECC	10927.2
8	ECC	11927.4
9	ECC	11198.9
10	ECC	11927.4
11	ECC	11927.4
12	ECC	11198.9
13	ECC	11198.9
14	UHPC	N/A

For quality control, multiple specimens were casted in a same batch and they were expected to have the same compressive strength. For instance, specimen No.3 and No.4 were casted at the same time, with a compressive strength of 9497 psi. Due to the limited amount of sensors, eight out of the fourteen specimens were fully covered with sensors on concrete and steel on both top and bottom. As a result, six of the specimens were monitored on selective locations. In fact, both ECC and UHPC provide high compressive strength, so when a particular specimen could not be fully covered with four sensors, the tensile region was the focus and the tensile responses were prioritized.

The data reflected high compressive strength of the materials. The average compressive strength of ECC was 11135.97 psi. Compressive strength of UHPC was not taken because of reasons discussed above and the expected value of compressive strength is 14000psi. The compression test proved that the mix design is adequate by showing a high compression strength. In addition, compressive strengths of the 11 specimens made of ECC were consistent without much fluctuation. This suggested that the experiment was done properly and the materials were able to fulfill their full functionality. Results in this section can be viewed as validation of mix design, equipment and experimental procedure. Figure 6.1 shows strength of the ECC specimens in compression.

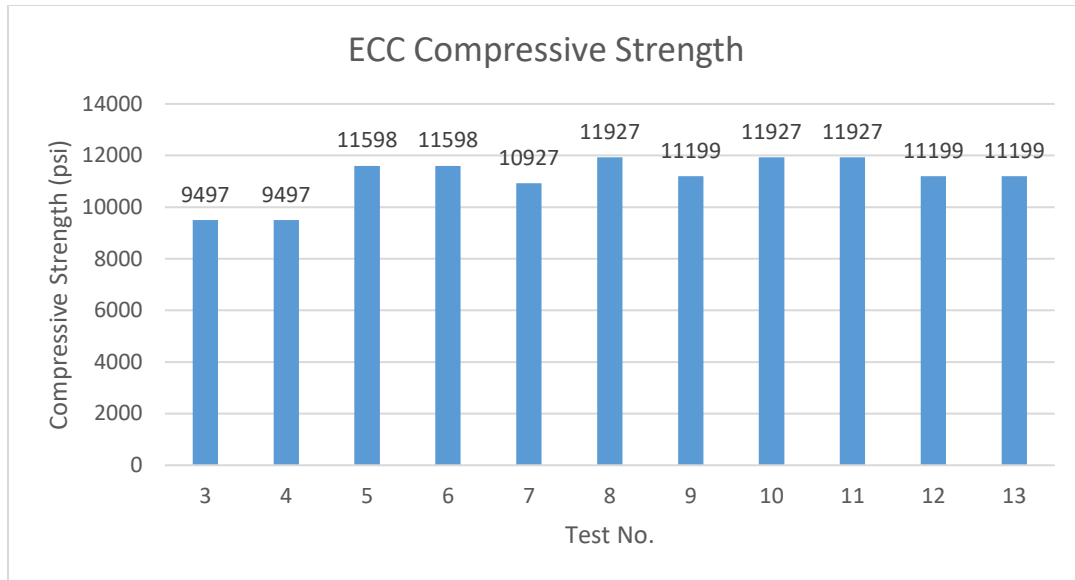


**Figure 6.1: ECC compressive strength**

### **6.1.3 Maximum tensile strain**

Strain readings were taken simultaneously with the applied loads and stresses. In fact, strain data cannot be treated the same as the applied loads and stresses. Unlike data for loads and stresses, which were directly read from the testing apparatus, the strain data relied on the compatibility between the concrete and the strain gauge. During data analysis, it was identified that some of the strain gauges experienced failure. Failure conditions included debonded sensor, damaged sensor or wire and fracture of the concrete specimen. Among them, the situation when the ECC or UHPC specimen fractured did not affect accuracy of the result because the sensor was not expected to return any data beyond this point. However, the other two conditions introduced uncertainties and the data must be analyzed with these potential sources of errors acknowledged. Although sensor failures might introduce disturbance in data, they are valuable to be studied and offered insights on areas of improvement of the

sensor system to ensure a successful field test in the future. This subject will be discussed in later sections.

Figures 6.2 and 6.3 shows the maximum tensile strength in concrete and steel of the 14 specimens. Note that “steel” here does not refer to reinforcing rebars. Due to high tensile strength of UHPC and ECC, conventional reinforcing steels are not required for strength. “Steel” in this section stands for sensors that were mounted on a steel plate and then placed on the concrete surface for strain data recording. In test No. 5, 6 and 8, strain gauges were only installed on steel plates; in test No. 8, 9 and 10, strain gauges were only installed on concrete; in test No. 4, the sensor system failed in steel. The results displayed a wide range of data with a minimum of  $171\mu\epsilon$  and a maximum of  $3155\mu\epsilon$  in concrete; a minimum of  $127\mu\epsilon$  and a maximum of  $725\mu\epsilon$  in steel. As mentioned above, strain data shown in this section could be disturbed by uncertainties resulted from the sensor systems. This will be discussed in detail in later sections.

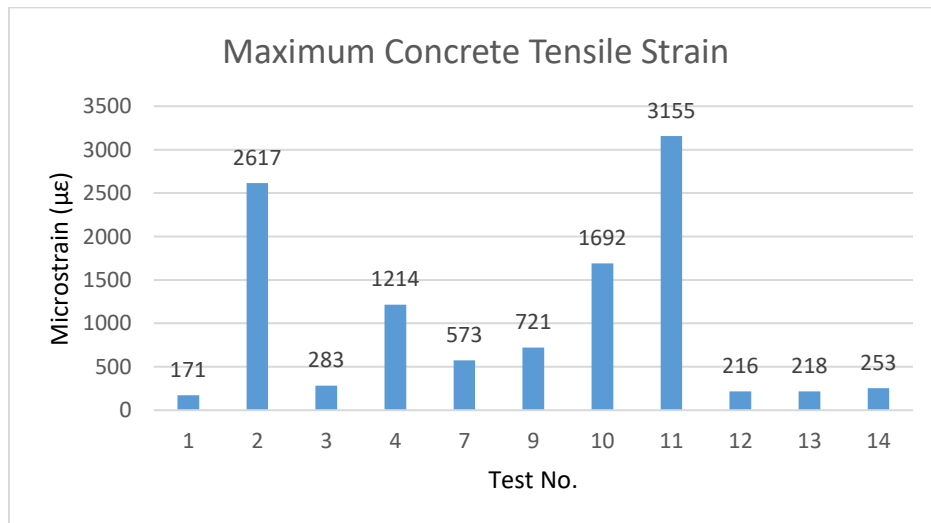


**Figure 6.2: Maximum concrete tensile strain**

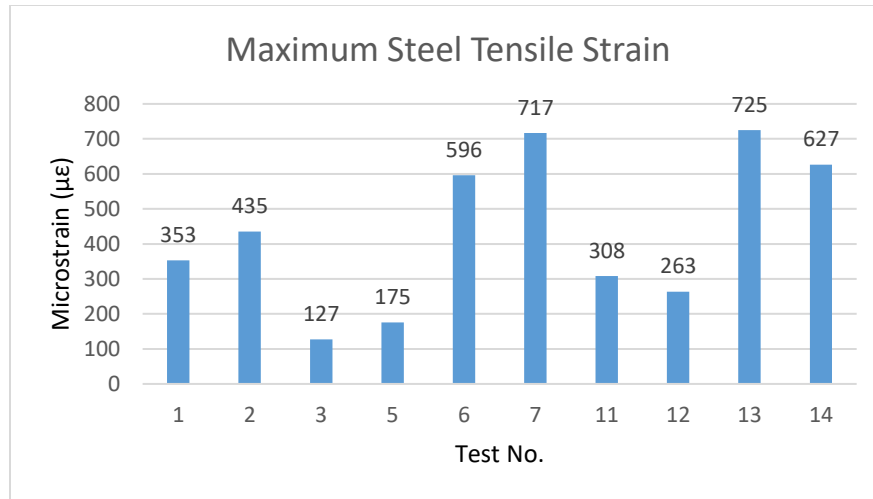


**Figure 6.3: Maximum steel tensile strain**

#### **6.1.4 Stress vs. Strain Curve**

Loads were applied in a cyclic pattern to the specimens. The specific number of cycles were not consistent among the 14 specimens, where some of the specimen experienced one cycle of loading while others had multiple. Overall, all the specimens displayed similar response so for illustration purpose, test No. 7 and No. 14 were selected to demonstrate experimental findings.

Figures 6.4-6.6 show the cyclic loading pattern, stresses and strains of specimen No. 14, which was made of UHPC. This particular specimen had undergone 14 cycles of applied loads with increasing magnitude. It can be identified that the response of the UHPC link slab specimen remained not affected by the number of repetitive loads applied because the stress and strain diagrams both reflected responses that were consistent to the loading pattern. No matter how many loading cycles the specimen had experienced, the UHPC link slab specimen was able to react

to the applied forces respectively until it fractured. This finding is consistent with the literature reviews and is critical to ensure the serviceability and reliability of the link slab.

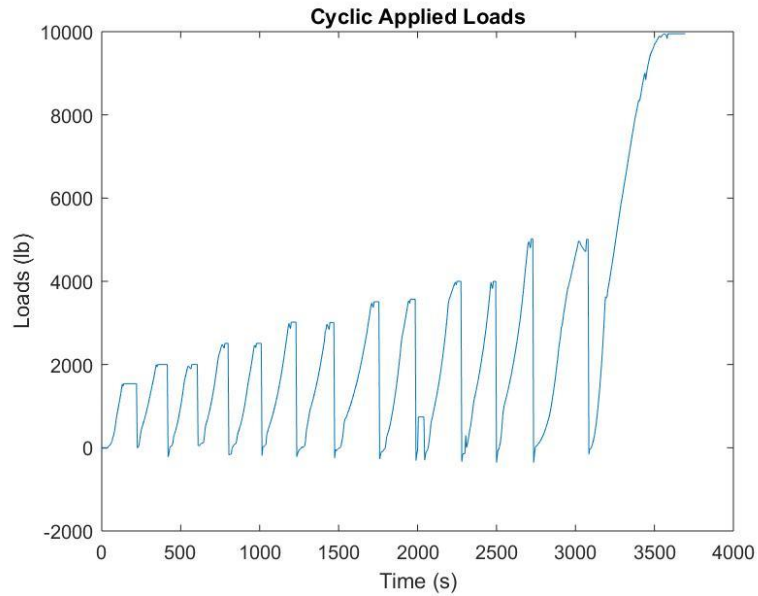


**Figure 6.4: Cyclic loading pattern of specimen No. 14 (UHPC)**

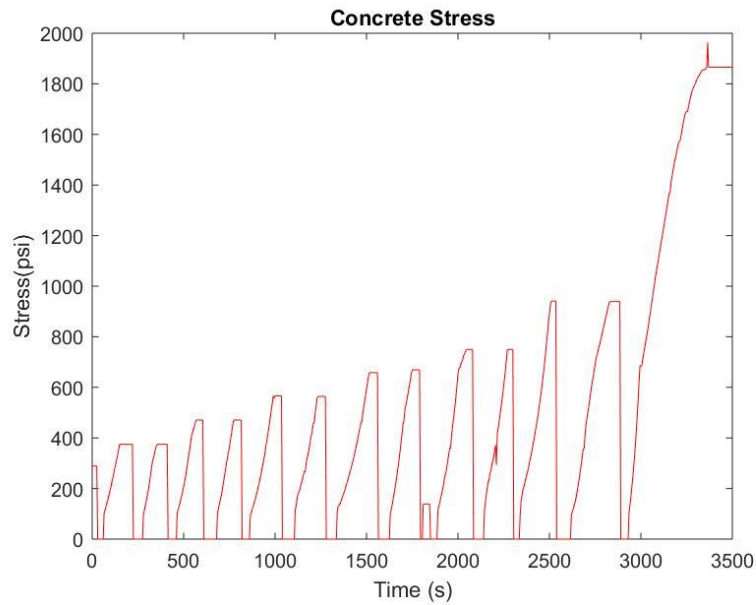


**Figure 6.5: Stresses of specimen 14 (UHPC)**

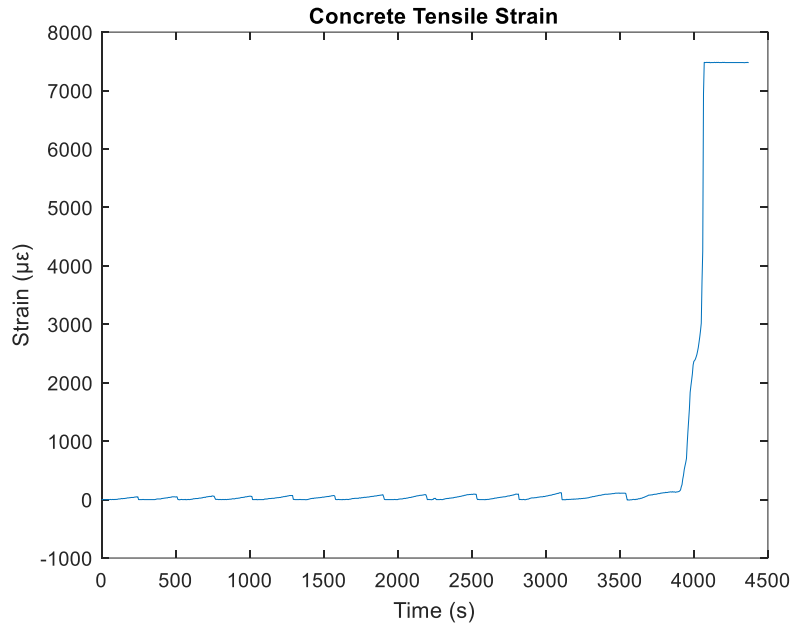


**Figure 6.6: Strains of specimen No. 14 (UHPC)**

To study the “metal-like” behavior of the UHPC and ECC materials, specimen No. 7 was selected to illustrate the findings. Specimen No. 7 was made of ECC and Figures 6.7 and 6.8 represent the applied loads and stresses during the experiment. Likewise, Figures 6.9 and 6.10 present the strain data on the specimen and the data were shown in two segments, where Figure 6.9 covers strains in the first 3 loading cycles and Figure 6.10 shows strains in the fourth and fifth loading cycles. Similar to the UHPC specimen, the trend and magnitude of the stress and strain data consistently matched the applied loads, during which the specimen was loaded five times with increasing loads until failure. This is consistent with the findings in the UHPC specimen and matches the claims reviewed in the literature.

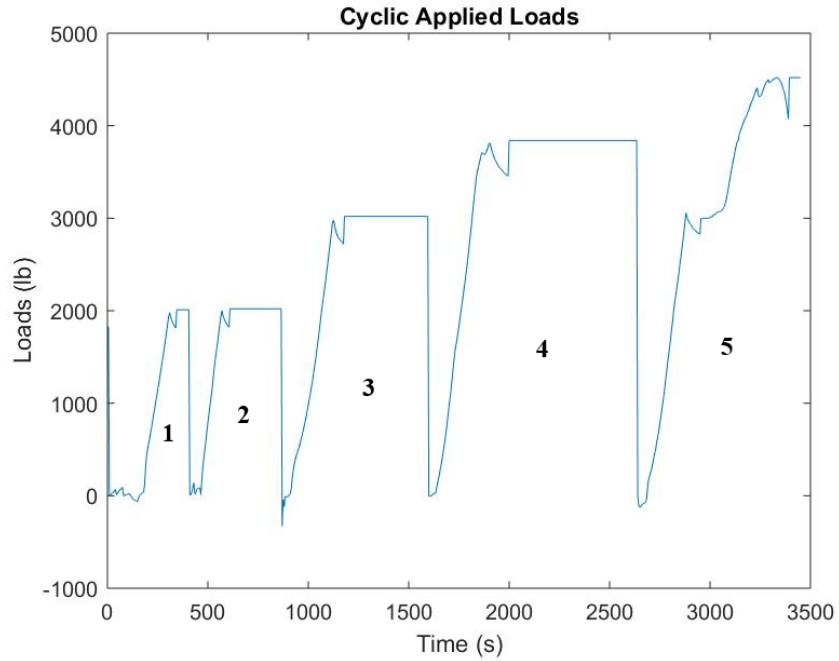


**Figure 6.7: Cyclic applied loads for specimen No.7 (ECC)**

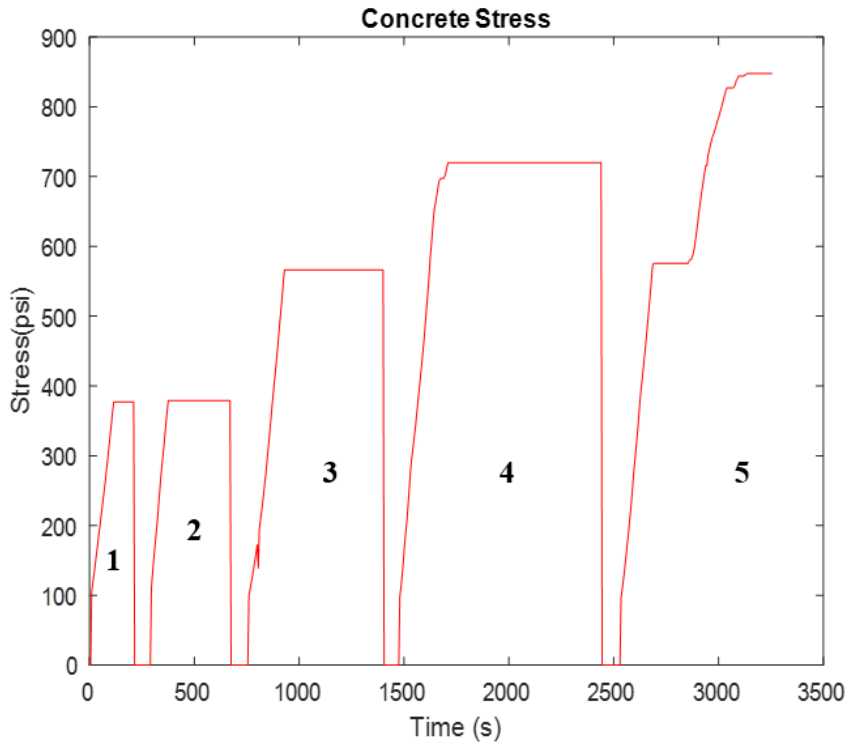


**Figure 6.8: Stresses on specimen No. 7 (ECC)**

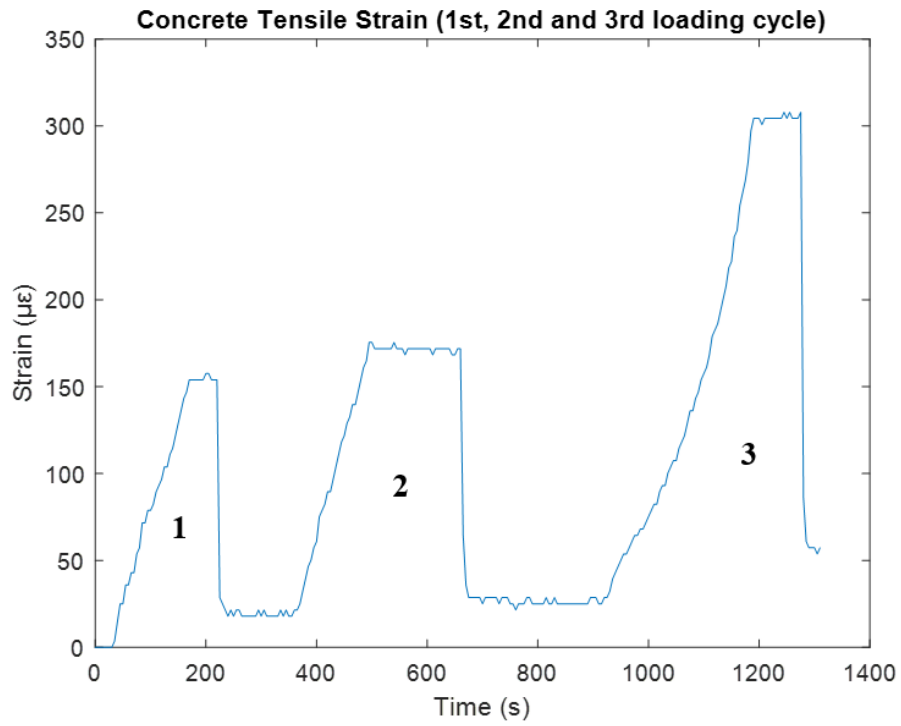


**Figure 6.9: Strain in first 3 loading cycles (ECC)**

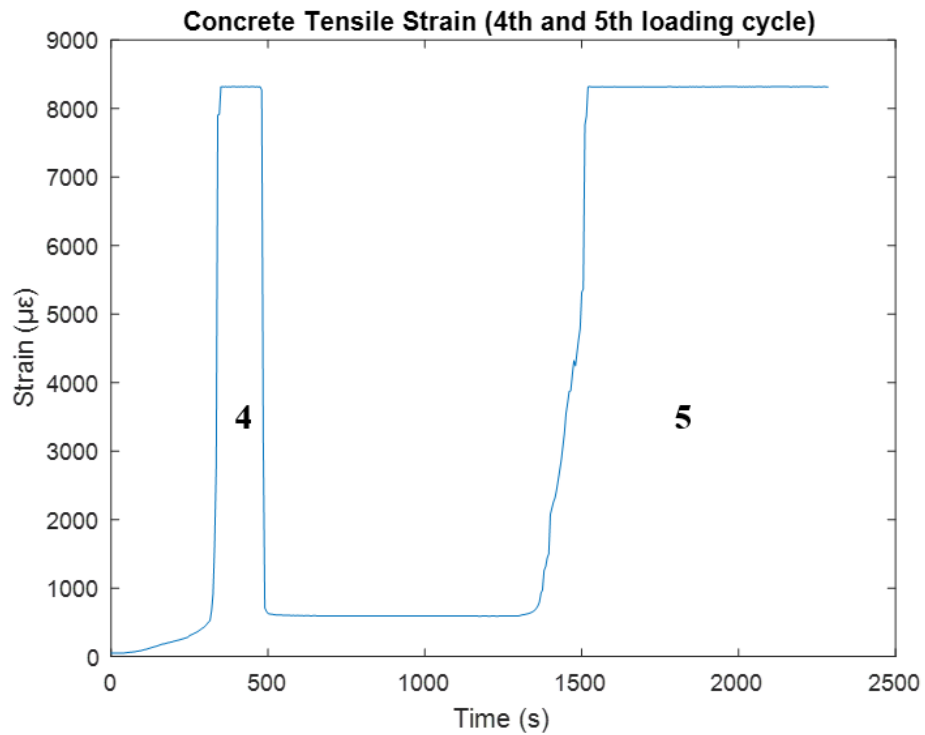


**Figure 6.10: Strain in 4th and 5th loading cycles (ECC)**

To illustrate the ductile behavior of the specimen, stress-strain diagrams were generated based on data shown above. During the first loading cycle there could be residual stresses presented and the last loading cycle experienced material failure. Thus, for accuracy, the second, third and fourth loading cycles were selected to be examined in this section. Moreover, the stress-strain curves were created using curve fitting tools in MATLAB and would only cover the linear elastic region of the specimen to show a clear demonstration of the material as it gradually entered the ductile region, where the strain kept increasing without much change in stress. Figures 6.10-6.12 show the results of the stress-strain curves using curve fitting. Equations 6.1-6.3 are the mathematical expression of the curves. All the curves were fitted using a second-degree polynomial model.

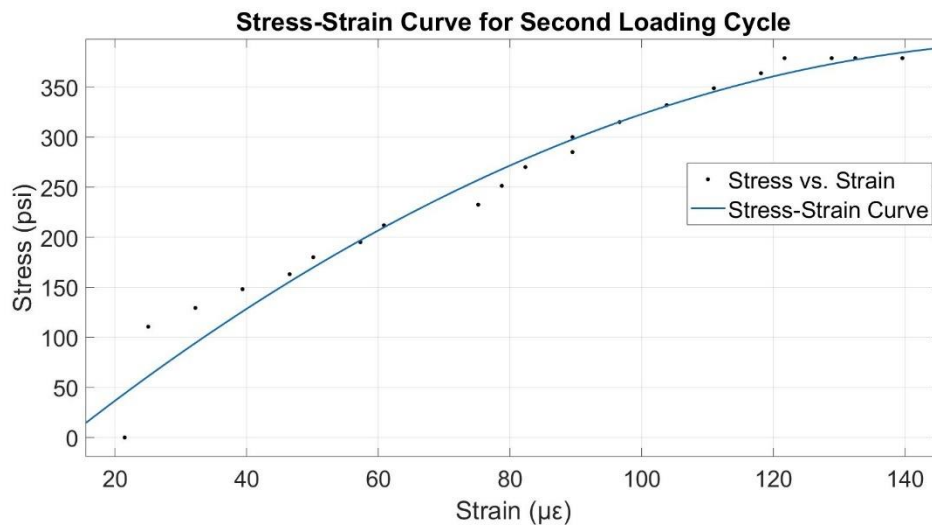


**Figure 6.11: Stress-strain curve for the 2nd loading cycle**

Where the curve can be described by:

$$f(x) = -0.01689x^2 + 5.605x - 68.74 \tag{6.1}$$

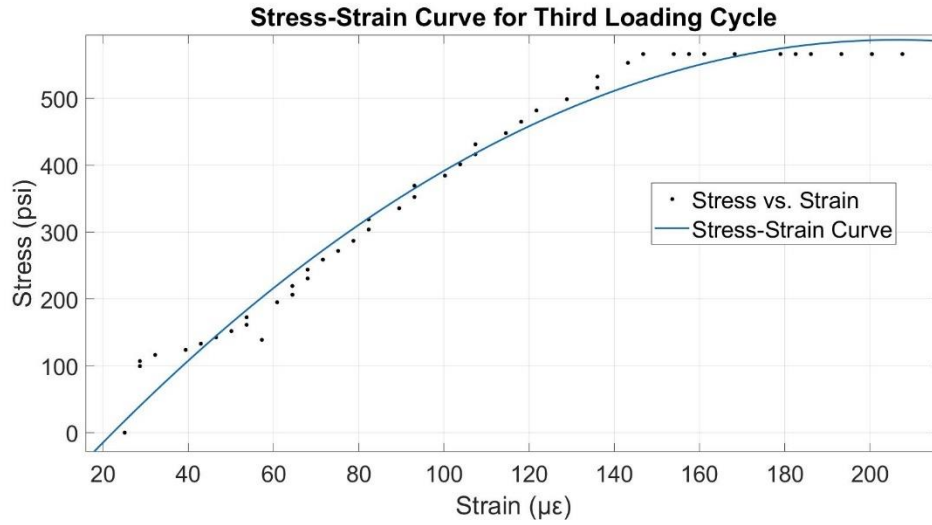


**Figure 6.12: Stress-strain curve for the 3rd loading cycle**

Where the curve can be described by:

$$f(x) = -0.01735x^2 + 7.16x - 151 \quad (6.2)$$

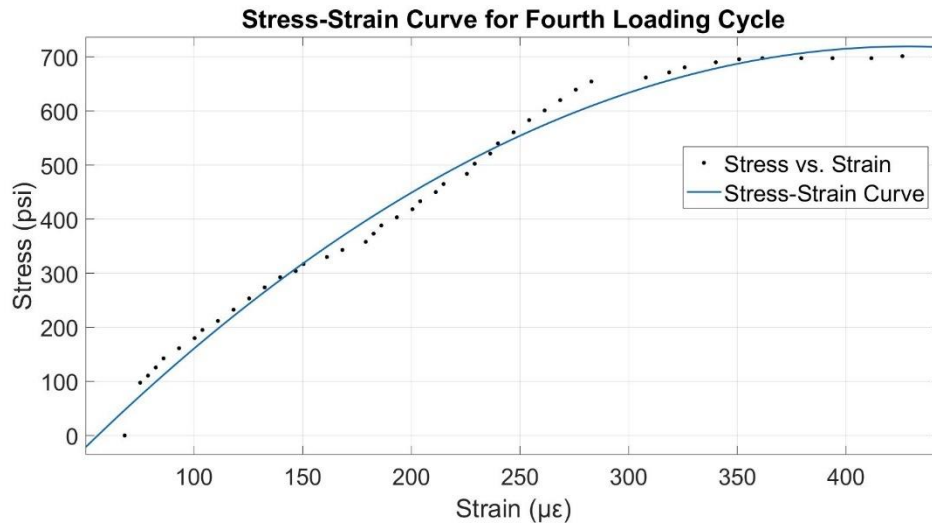


**Figure 6.13: Stress-strain curve for the 4th loading cycle**

Where the curve can be described by:

$$f(x) = -0.005165x^2 + 4.43x - 230.6 \quad (6.3)$$

According to the stress-strain curve, it is clear that the specimen gradually entered the ductile region as the slope started to gradually decrease.

## **6.2 Results on Sensor Performance**

### **6.2.1 Sensor Performance Criteria**

As discussed in previous chapters, there were two types of sensor configurations. One is the direct approach, meaning that the strain gauge was directly placed on the concrete specimen on designated locations. The other type of configuration is by mounting the strain gauge to a steel plate before installing them on the concrete specimen. Performance of the sensor systems were compared in this section to identify potential areas for improvements.

A satisfactory sensor system should have the following characteristics: consistency and compatibility. Consistency requires the sensor to be reliable, sending continuous data point. Compatibility means that sensors in the two configurations should provide data that share the same trend and are close to each other because the strain gauges were used to measure the strain within the same region over the concrete specimen.

### **6.2.2 Sensor Survival Rates**

Reliability and accuracy of the sensors have great impact on interpretations from the lab tests. As previously discussed, one of the purposes of this experiment was to serve as a pilot project in order to evaluate the feasibility and material properties. Therefore, performance of the sensors were recorded and evaluated in this

section to provide a review of the experiment and offer recommendations for future field tests. Table 6.2 summarizes sensor failure and survival rate for each the test. The average survival rate was calculated as , with a lower bound of 50% and an upper bound of 100%. This is acceptable since this is the first attempt in sensor system design and arrangement.

**Table 6.2: Senor failure and survival rates**

Test No.	Material	No. of Sensors	Failure Sensor Location	No. of Sensor Failures	Failure Rates (%)	Survival Rates (%)
1	UHPC	4	None	0	0	100
2	UHPC	4	None	0	0	100
3	ECC	4	Bottom Concrete, Top Concrete	2	50	50
4	ECC	4	Bottom Concrete, Top Concrete	2	50	50
5	ECC	1	None	0	0	100
6	ECC	1	Embedded Bottom Steel	0	0	100
7	ECC	4	Bottom Concrete	1	25	75
8	ECC	2	None	0	0	100
9	ECC	3	Bottom Concrete	1	33.3	66.7
10	ECC	2	Bottom Concrete	1	50	50
11	ECC	4	Bottom Concrete	1	25	75
12	ECC	2	None	0	0	100
13	ECC	4	Embedded Steel	1	25	75
14	UHPC	4	Bottom Concrete	1	25	75

### **6.2.3 Sensor Failure Due to Lost Connection**

It was noticed that some of the sensors did not completely fail. Some of the sensors were able to recover. In other words, temporary loss of connection was observed in the sensor systems. Figure 6.13 shows an example of this situation.

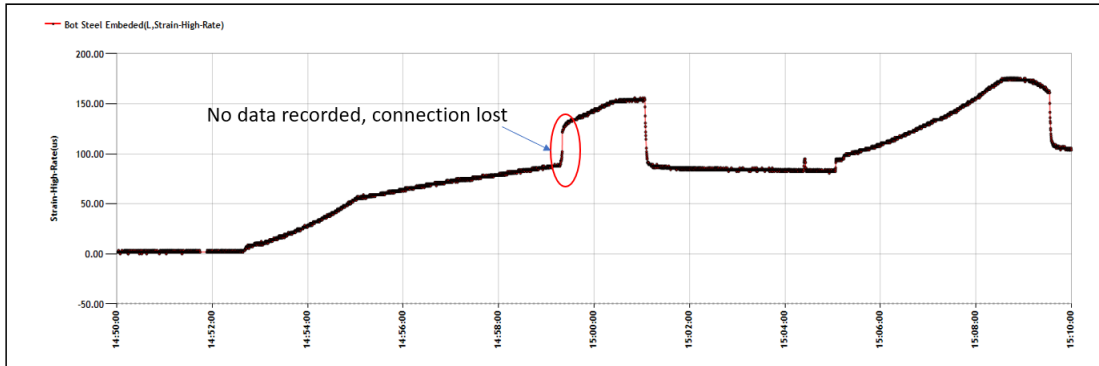


**Figure 6.15: Temporary loss of connection in sensors**

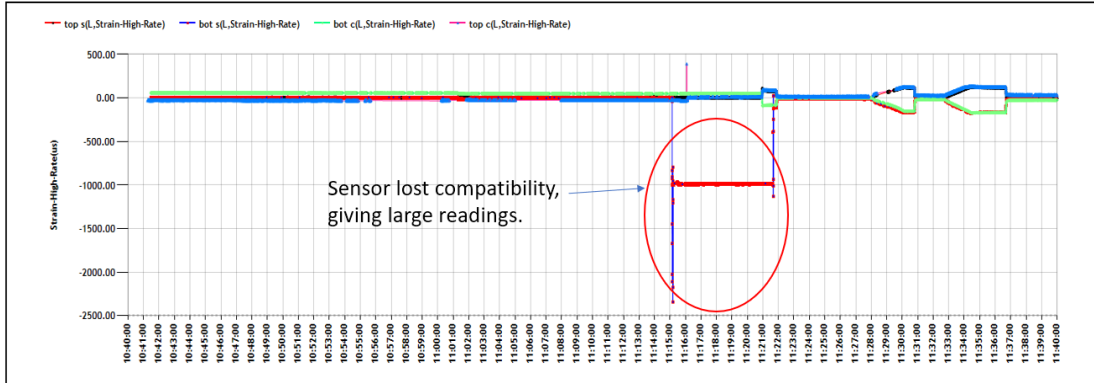
There were two sensors next to each other, measuring strains in the same area. In theory, readings from the two sensors should be identical or within an acceptable range. However, it is clear that some of the data were missing in the middle of the test. But the data recording resumed shortly after this point. The graph also shows a few other locations where some of the strain data were missing, making the data line discrete. Note that this sensor system was attached to a metal plate before it was installed on the concrete specimen.

### **6.2.4 Sensor Failure when reaching a certain level of strain**

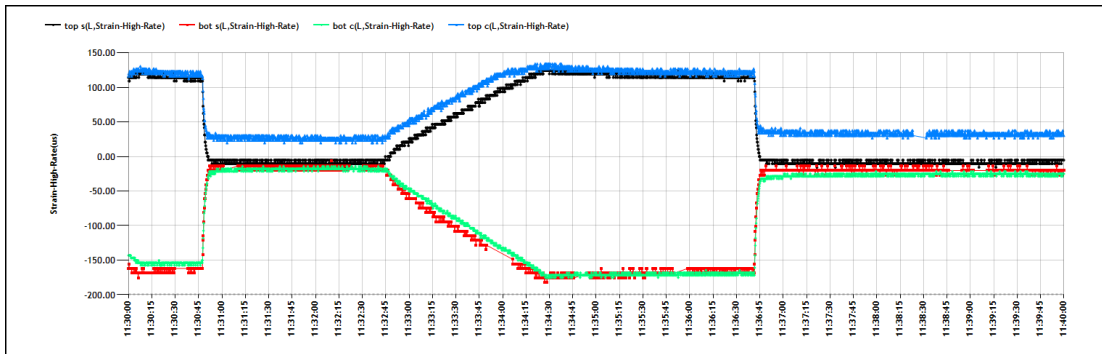
Another failure situation is when the strain gauge returned readings that were not reasonable, indicating failures in the sensor system. However, in this case, the sensor could still recover after a short period of time and resume taking readings.

Figure 6.14 and 6.15 describes the condition discussed above. In Figure 6.14, sensors

on mounted on steel plates lost compatibility with the sensors directly installed on concrete, sending enormous readings of strain. However, Figure 6.15 proves that the two sensors were able to recover compatibility shortly after.



**Figure 6.16: Temporary loss of compatibility**



**Figure 6.17: Compatibility between sensors recovered**

### **6.2.5 Complete Sensor Failure**

Sensor failure is defined as the sensor's inability to provide any readings of strains. This could happen in the middle of the test or even at the start of the test.

Figure 6.18 is an example of sensor failure.

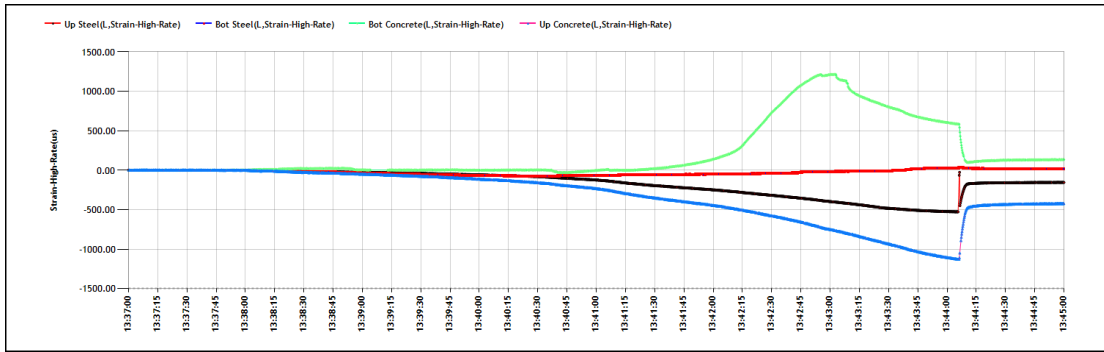


**Figure 6.18: Sensor failure from the start of the test**

Based on the plot, the sensor with steel plate mounted on the top concrete position (shown in red line) was barely able to capture any readings throughout the entire test. While the one without a steel plate in the same location (shown in black line) had taken strain data. It is clear that not only this particular sensor had lost its compatibility with the other sensor, but also failed to record any strain on the concrete specimen.

### **6.2.6 Possible Causes for Sensor Disturbance and Failures**

Failure of the sensor system could be attributed to a variety of reasons. However, it was identified that most of the disturbance and failures occur on sensors that were mounted on a steel plate, as 88.8% of the failures took place on them. While sensor failure on strain gauges without a metal plate was only 11.2% among all the failure cases. The results demand better understanding on connection of sensor with an intermediate material before placing it on a structural member.

One possible cause of disturbance is the cracks development during the bending test. As fine cracks started to developed and gradually formed a major fracture plane, it is possible that the movement would have been disruptive to the

nearby sensors, causing them to lost connection or compatibility. Another reason could be deflection of the specimen. Because of the high tensile ductility of the ECC and UHPC specimen, deflection could be large enough distorting wire connections within the sensor system, causing them to be temporary dysfunctional. Due to the scale of the concrete specimen, not major deflection was observed so that sensor disturbance caused by deflection should only be resulted in temporary loss of connection or compatibility. Besides, human errors are another potential source of errors. It is possible to introduce errors during the installation of the sensor systems. However, the effect of this cause should be minimal as all the strain gauges were treated properly and with great curtain. Similarly, defects in sensors could not be ruled out even though the possibility is minimal.

### **6.2.7 Recommendation on Sensor Application**

Despite sensor disturbance and failure, the system is considered as reliable in a feasible range of measurement. Figure 6.19 shows a moment when the two sensors lost combability. Table 6.3 summarizes strain levels at which the sensor lost compatibility.

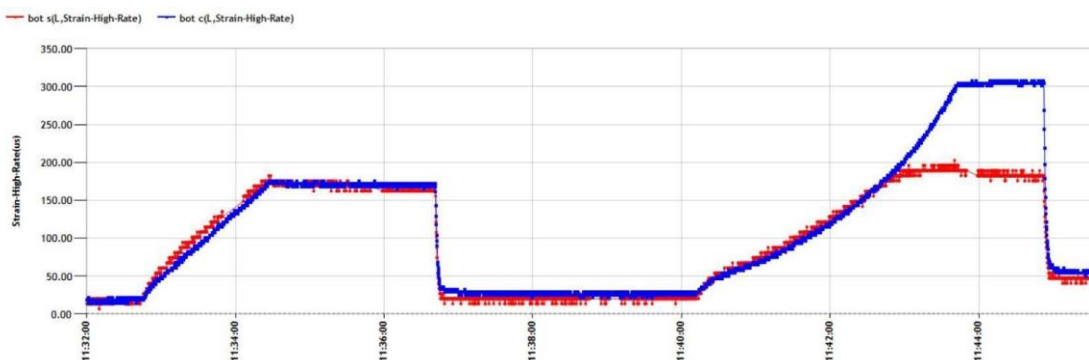


**Figure 6.19: Point of lost compatibility**

**Table 6.3: Strain level of lost compatibility**

Test No.	Material	No. of Sensors	Divide in Compression (microstrain)	Divide in Tension (microstrain)
1	UHPC	4	821.61	143.2
2	UHPC	4	891.41	304.3
3	ECC	4	114.56	71.6
4	ECC	4	934.38	Sensor failure
5	ECC	1	N/A	N/A
6	ECC	1	N/A	N/A
7	ECC	4	338	200.48
8	ECC	2	332.94	N/A
9	ECC	3	N/A	819.82
10	ECC	2	N/A	N/A
11	ECC	4	N/A	195.03
12	ECC	2	N/A	123.51
13	ECC	4	N/A	134
14	UHPC	4	304.44	212.74

Based on experimental results, there exists a linear relationship between the two types of sensor systems: sensors directly mounted on concrete and sensors attached to a steel plate before they are installed on concrete. In compression, the maximum feasible range was recorded as  $340 \times 10^{-6}$  in ECC and  $890 \times 10^{-6}$  in UHPC; in tension, the feasible measurements were up to  $200 \times 10^{-6}$  in ECC and  $304 \times 10^{-6}$  in UHPC. When the specimen experienced a strain that exceeds the value presented above, the sensors will lose compatibility and cannot be calibrated. Under compression, strain data calibrated using respective coefficient factors were within the range of feasible range of measurement for both UHPC and ECC. On the

contrary, the factored tensile strain in UHPC and ECC generally exceeded the feasible range of measurement. In order to solve this problem, nonlinear analysis is needed to address the incompatibility of the sensor with steel plates in regions of high tensile strain. Despite the present of this discrepancy, the experiment is considered successful by providing details of the sensor and material properties and offering guidance for future improvements.

### **6.3 Fine Crack Development**

One of the advantages in material properties of ECC and UHPC is the ability to form fine cracks across the width of the specimen. Fine crack allows ECC and UHPC link slabs to limit the amount of water penetration, protecting the girders and other substructures. By developing fine cracks ECC and UHPC are also able to sustain deformation with large curvature and display high tensile ductility.

Cracks on the 14 concrete specimens were recorded by photos. Most of the cracks were hairline in width until multiple fine cracks formed a major fracture plane when the specimen was loaded to failure. Figures 6.20 to 6.22 are cracks overserved on the concrete specimens. For better visibility, the cracks were first painted in blue inks. The results are satisfactory because the specimens were able to develop fine cracks along the width. The width of the cracks overserved is small enough to limit the amount of water penetration into the concrete, therefore providing a better protection for the member and substructures.



**Figure 6.20: Fine cracks on an ECC specimen.**



**Figure 6.21: Fracture plane formed by fine cracks on a UHPC specimen**



**Figure 6.22: Fracture plane formed by multiple fine cracks (ECC)**

Although high tensile ductility was observed in both ECC and UHPC materials, it was evident that specimens made of ECC were generally more ductile than those made of UHPC. On most of the ECC specimens, cracks were developed more gradually and there were a larger number of fine cracks on the specimen. On the other hand, UHPC materials tend to have more concentration in crack development where most of the fine cracks occurred in the center of the specimen, in which the moment was the greatest.

## Chapter 7 Discussion

### 7.1 Lab Test

Overall, experiments conducted in the are successful. The material properties of ECC and UHPC were studied, including compressive strength, tensile ductility and fine crack propagation. Nevertheless, there is room for improvement. First of all, a thinner geometry can be used in the production of the concrete specimens. An example can be seen in Figure 7.1. By reducing the depth of the specimen to be considerably smaller than the width of the concrete slab, this type of geometry is able to convey the high tensile ductility of ECC and UHPC more effectively. A thinner slab can be monitored in terms of its vertical deflection to describe its ductility under a bending test. Vertical deflections prior and after the test can be compared to indicate the material's ability to resist permanent deformation in response to stress. In this case, a stress-strain curve that is closer to a metallic material is also expected.



**Figure 7.1: Thin slab showing ECC tensile ductility**

## 7.2 Sensor Protection

Sensor performance are satisfactory, considering this is the first trail using the SenSpot™ strain gauge on concrete materials. Conventionally, this specific sensor is generally used on structural steel members. Uniquely, possibility of expanding the use of the sensor into concrete materials are explored in this project. The SenSpot™ strain gauge were used on both ECC and UHPC specimens in the lab test and are also planned to be installed on the bridge in field test for long-term monitoring.

One of the biggest challenges associated in the use of the SenSpot™ strain gauge is sensor protection. A potential source of distortion is crack developed on concrete, compared to steel that does not crack. Cracked concrete can led to damage in wires and the strain gauges, resulting in lost communication between the sensor and the data acquisition system. For the purpose of long-term monitoring, this is not ideal because consistency and continuity in data recording is essential. Another potential threat is the vulnerability of the sensor system when exposed to the environment. Despite exterior coating on the wires, a full cycle of four seasons and various weather conditions could potentially introduce damage to the wires and transmitters that are exposed to the environment. However, the devices can be substituted from back up storage if any failure is identified.

### 7.3 Evaluation of Sensor Performance

According to experimental data, the survival rate of the sensor systems in the lab test is 76.7%. Figure 7.2 summaries this result. For a first trail, the result is acceptable. Specifically, strain gauges mounted on a piece of steel plate proved to be significantly more reliable than those directly installed on concrete. This finding validates the design of the sensor system for the field test. However, an improved design of the sensor system is still being developed. Possible adjustment includes thinner and smaller metal for reduced uncertainty; and alternative options for wire protection.

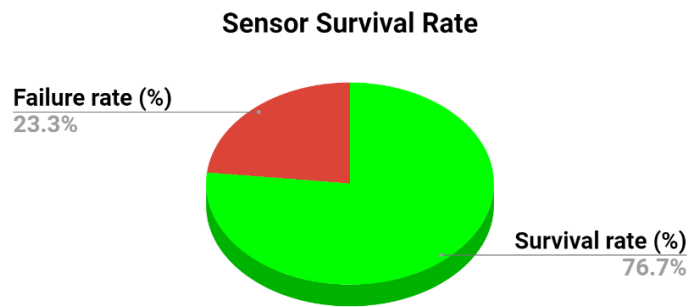


Figure 7.2: Overall sensor survival rate

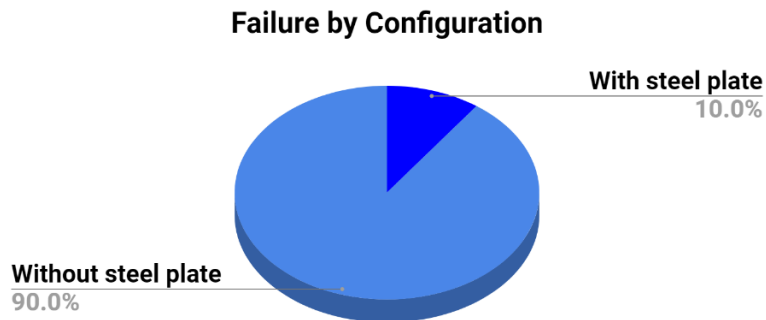


Figure 7.3: Survival rate by configuration

# Chapter 8 Conclusion and Future Work

## 8.1 Conclusion

It is common to design bridges as simple span structures with expansion joints between adjacent spans. However, chloride-contaminated water penetration and debris accumulation have been causing issues in bridge maintenance and rehabilitation. To solve this problem, link slab has emerged to become a desirable option in recent years. By replacing conventional expansion joints with a continuous concrete link slab that connect two adjacent spans, the amount of water infiltration and debris accumulation can be massively reduced so the supporting girders and substructures can be better protected. Meanwhile, application of link slab allows the bridge spans to remain simply-supported. Furthermore, flexural stiffness of the link slab is significantly smaller than that of the supporting girders so that it will introduce negligible amount of flexural stiffness to the system. Moreover, stiffness of the link slab can be further reduced by add a 5% debonded zone between the link slab and the girders underneath. Nevertheless, link slab will not solely solve issues of structurally deficient bridges. Link slab is more suitable in rehabilitation for older bridges. For bridges that are structurally deficient, a combination of engineered approaches is needed to protect the structural integrity of the bridges.

For link slab application, certain material properties must be satisfied: high strength for structural integrity; high tensile ductility to ensure serviceability and reliability under service traffic loads; limited crack width. To meet the above

specifications, ECC and UHPC are adopted for constructing link slabs. Both ECC and UHPC provide high strength and tensile ductility, with fine cracks in the longitudinal direction. To study performance of link slab using ECC and UHPC, two finite element models were generated to simulate original bridge performance; experiments were conducted to learn about material properties of ECC and UHPC; sensor performance was evaluated for recommendation to future applications. Presented in this section is a summary of the conclusions made based on results obtained in this research project:

1. Overall, ECC specimens show high strength, with an average compressive strength of 11135.97 psi for the 11 ECC specimens. Strength of the three UHPC specimens were not directly recorded because they were mixed strictly based on specifications provided by the manufacturer. According to the manufacturer, the average compressive strength of UHPC is 14000psi. The high strength of ECC and UHPC ensures the link slab's ability to meet specifications in bridge loading criteria.
2. Responses and performances of the link slab specimens are independent to the number of cyclic loadings applied. This result reflects the reliability and predictivity of the link slab.
3. Ductile performances were achieved during the three-point bending tests. A "yield" point was observed in the stress-strain curve, reflecting the "metal-like" property of the ECC and UHPC material. This finding verifies the high tensile ductility of the material.

4. Performance of sensor systems in the lab are overall satisfactory. While disturbance and failure exist.
5. Feasible range for measurement of the strain gauges is  $340 \times 10^{-6}$  in ECC and  $890 \times 10^{-6}$  in UHPC under compression;  $200 \times 10^{-6}$  in ECC and  $304 \times 10^{-6}$  in UHPC under tension. Beyond this range, sensor systems will lose compatibility.
6. Fine cracks developed on the ECC and UHPC specimens are hairline in width across the longitudinal direction on the specimens. The width of the fine cracks is narrow enough to efficiently protect the supporting girders and other substructures from damage caused by water penetration. Hence, the results support that link slab made of ECC and UHPC is effective on preventing damage due to leakage.

## **8.2 Future Work**

Further study needs to be done to further improve the knowledge of link slab in terms of application on actual bridge structures. The following list summarizes the proposed future work of this research project:

1. Structural response of the bridge under standard truck loads need to be collected and compared with the results measured in field test.
2. Plots of strain distribution of the link slabs need to be generated based on data recorded in the field test.

3. A better design is required to improve stability of the sensor system in terms of its performance.
4. Nonlinear analysis is needed to calibrate sensor incompatibility when the readings exceed range of feasible measurement.
5. More experiments can be performed to specifically focus on the high tensile ductility of ECC and UHPC. For instance, thinner specimens (one dimension of the specimen is considerably larger than the other, similar to a “deep beam”) of ECC and UHPC can be produced for a better visualization of the “metal-like” behavior under bending, where the material shows large tensile ductility. Deformation with large curvature under bending is more obvious in a thin member and this is going to help demonstrating the high tensile ductility of ECC and UHPC.
6. Link slabs can be implemented into the finite element models to simulate long-term response of the bridge.

# Appendix: Bridge Thermal Analysis

## 1. THERMAL STRESSES

If the structural element is restrained from movement then a change in temperature will lead to thermal stresses. Changes in the uniform temperature generally only lead to thermally induced stresses in statically-indeterminate structures. Thermal gradients that are nonlinear over the cross section will result in the development of thermally-induced stresses in both statically determinate and indeterminate structures. These nonlinear thermal gradients will induce self-equilibrating stresses in the bridge superstructure.

### *a. Self-Equilibrating Stress*

The nonlinear variation of temperature along the depth of the bridge will produce nonlinear strain. But as plane sections tend to remain plane so the final strain profile must be linear as per the Navier-Bernoulli hypothesis. This will cause a strain difference. The difference between these strains will result in self equilibrating stresses.

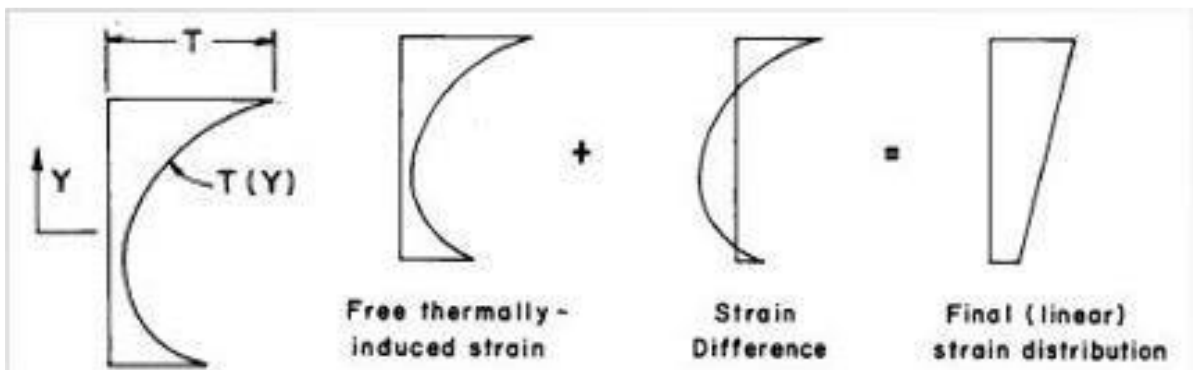


Figure 1 Strain Difference causing self-equilibrating stresses

The heating and cooling of steel girder systems with composite bridge decks was analyzed. Due to the differences in thermal expansion coefficient and different exposure to radiation, convection and conduction, the heating and cooling of a composite girder cross-section is non-uniform. If both the deck and the girder, are restrained in the same place, thermal stresses will be induced due to the uneven heating and cooling of the structure. Accounting for these additional stresses through increases in material strength, flexible piles, hinged abutments, and/or bearings could help alleviate stresses in this local behavior.

## **2. NCHRP REPORTS REVIEW**

### ***a. NCHRP 20-07/106 - Thermal Movement Design Procedure for Steel and Concrete Bridges (2002)***

This report was submitted by Charles w. Roeder in 2002. This report provides us the methods to calculate the maximum and the minimum design temperatures for steel and concrete bridges throughout the US. Two simplified methods (Emerson and Kuppa) were developed to estimate the average bridge temperature since the actual calculation of bridge temperature distribution is complex. The results obtained from these methods were compared to the limited field measurements available. This comparison showed that the Kuppa method provided better estimates of the extreme average bridge temperatures. Since we use extreme temperatures for 5 determining bridge design movements the Kuppa method was considered to produce design maps. Emerson method was conservative compared to the Kuppa method. Historic weather

data was combined with Kuppa method to create design maps for the maximum and minimum average bridge temperatures for steel girder bridges with concrete decks and concrete girder bridges with concrete decks. The design maps showed that composite steel bridges can be designed for smaller movements than recommended by procedure A in AASHTO specifications. The design maps were introduced in AASHTO as procedure B under uniform temperature change. Kuppa method used extreme events to calculate the average temperature since these extreme events control the thermal design. The temperature distribution within the bridge will depend on time and the type of bridge. They proposed a formula to calculate the average temperature  $T_{Avg}$ . This method included all the properties of the bridge along with conduction, convection and radiation heat transfer.

$$T_{avg} = \frac{\sum A_i E_i \alpha_i T_i}{\sum A_i E_i \alpha_i}$$

Where

$i$  = different segments of the bridge

$A_i$  = Cross sectional area of the  $i$ th segment

$E_i$  = Elastic Modulus of the  $i$ th segment

$\alpha_i$  = Coefficient of thermal expansion of the  $i$ th segment

$T_i$  = Temperature of the  $i$ th segment

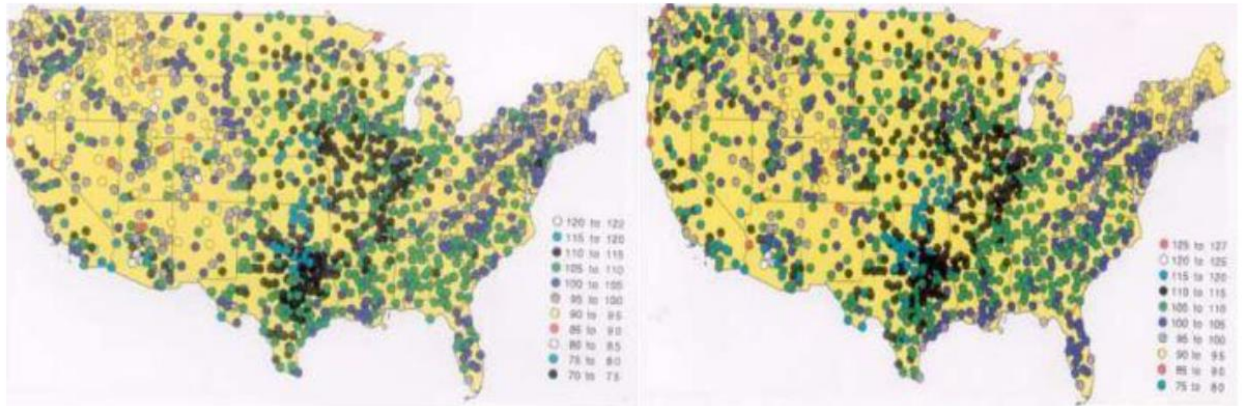


**Figure 2: Maximum average temperature of bridges by 1. Emerson 2. Kuppa methods**

The comparison between average maximum temperature of bridges calculated by both methods show similar temperature ranges. These figures show that there are consistent trends for average bridge temperatures. Emerson method is consistently conservative in predicting extreme low temperatures. It predicts a lower minimum extreme temperature when compared to the Kuppa method.

Bridge Type	Temperature Range, $\Delta T$ , Inferred from Displacement Measurements	Temperature Range Predicted by Design Map of this Report
Steel Girder Bridge with Concrete Deck	138 <sup>o</sup> F	147 <sup>o</sup> F
Precast Concrete Girder Bridge	110 <sup>o</sup> F	130 <sup>o</sup> F
Concrete Box Girder Bridge	107 <sup>o</sup> F	130 <sup>o</sup> F

**Table 1: Temperature variation for bridge types**

The proposed design maps were verified with the measured field data in Minnesota. The previous AASHTO specifications provided lower values for the

temperatures. The new contour design maps were used to estimate the maximum and minimum temperatures and they are compared to the values of temperature ranges calculated from the measured field displacements. The measured temperature ranges were within the temperature ranges provide by the design maps.

***b. NCHRP Report 276, Thermal Effects in Concrete Bridge Superstructures, (Imbsen et al., 1985)***

This report provides us the proposed design criterion for thermal gradients for concrete bridges. Several concrete precast bridges were studied in this case study under various thermal gradients taken from several codes around the world. The report is a comprehensive study of thermally induced stresses in concrete bridge superstructures. The stresses resulting from average temperature have an important effect while the stresses developed due to thermal gradients effected the bridges in only some cases. Previously most bridges have been designed to accommodate only the longitudinal movement caused by uniform temperature change. But In this report several bridges were evaluated under various thermal gradients taken from US and foreign countries. The thermal gradients used in this report were from New Zealand, England, Ontario and US. Although AASHTO didn't specify a thermal gradient in 1985, the gradient used by PTI (Post Tensioning Institute) was used on behalf of the US. The following concrete bridges were considered for the case studies.

Table 5. Summary of bridges included in case studies for longitudinal temperature effects.

CASE NO.	NAME/LOCATION	SUPERSTRUCTURE	SUBSTRUCTURE	LONGITUDINAL DIRECTION		DEPTH/SPAN RATIO	NO. SPANS	NO. HINGES	NO. FRAMES	COMMENT
				LENGTH	DEPTH					
1L	Colorado River Bridge California/Arizona	Precast, prestressed I-girder	Pier Wall	565 ft-6 in.	6 ft-3 in.	0.056	5	0	1	Representative I-girder
2L	West Silver Eagle Rd. Overhead, California	Cast-in-place prestressed box girder	Double Column	750 ft-0 in.	5 ft-0 in.	0.037	6	0	1	Representative box girder
3L	Turkey Run Creek Br. Indiana	Precast, prestressed segmental box girder	Single Column	317 ft-0 in.	9 ft-0 in.	0.057	2	0	1	Segmental cantilever
4L	Kishwaukee River Br. Illinois	Precast, prestressed segmental box girder	Single Column	1,096 ft-0 in.	11 ft-8 in.	0.047	5	0	1	Segmental cantilever
5L	Columbia River Br. Washington	Cast-in-place prestressed segmental box girder	Single Column	1,870 ft-0 in.	9 ft-0 in. min. 24 ft-0 in. max.	0.053	5	0	1	Segmental & haunched cantilever
6L	W. Silver Eagle Rd. OH (Falsework) California	Cast-in-place prestressed box girder	Double Column	750 ft-0 in.	5 ft-0 in.	0.037	6	1	2	Falsework loading
7L	East Connector California	Cast-in-place reinforced box girder	Single Column	1,104 ft-0 in.	6 ft-0 in.	0.055	11	2	3	Multiframe
8L	Miller Creek F-11-AK Colorado	Precast, prestressed segments/box girder	Single Column	443 ft-3 in.	8 ft-0 in.	0.041	3	0	1	Case history

Figure 3: Bridges used for case studies

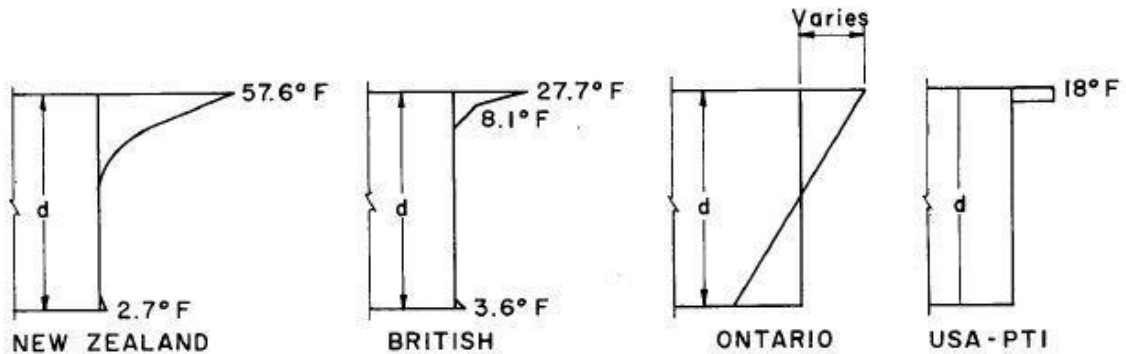
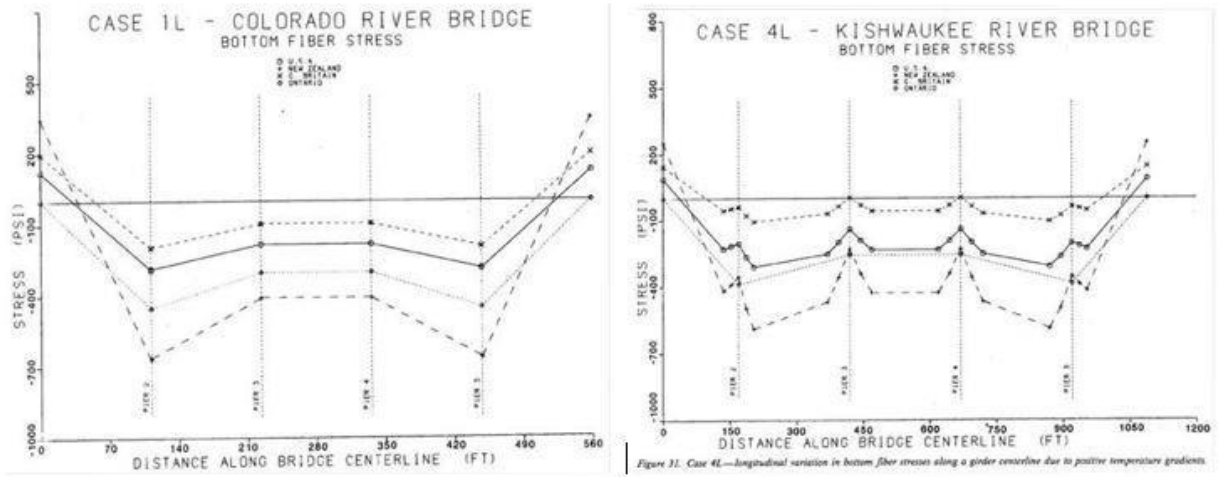


Figure 16. Thermal gradients used for case studies.

Figure 4: Thermal Gradients Used for the Case Studies

The results from stress diagrams showed that some conditions influence the values significantly. The following stress diagrams show the effect of bottom slab flare and monolithic column on bottom fiber stresses. The presence of bottom slab

flare near reduced the stress values where the thickness is maximum. The values of the top fiber stresses did not show any sudden change since there is no flare present.



**Figure 5: Bottom Fiber Stress values 1. No Bottom Slab Flare 2. Bottom Slab Flare**

Effect of monolithic column on the stresses is shown in the following figure.

The values near the supports reduced significantly.

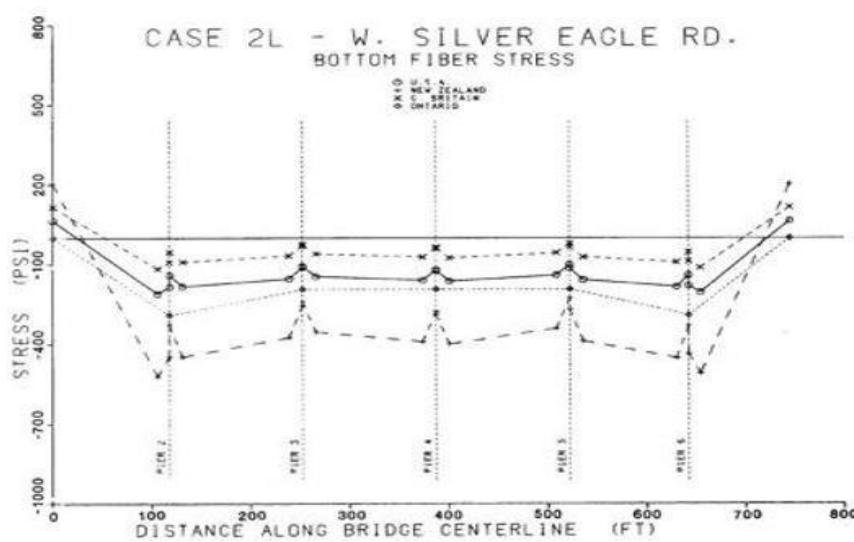


**Figure 6: Effect of monolithic column on bottom fiber stresses**

The presence of a hunched girder also significantly varies the stress values.

The bottom fiber stress values are maximum where the depth of the girder is least.

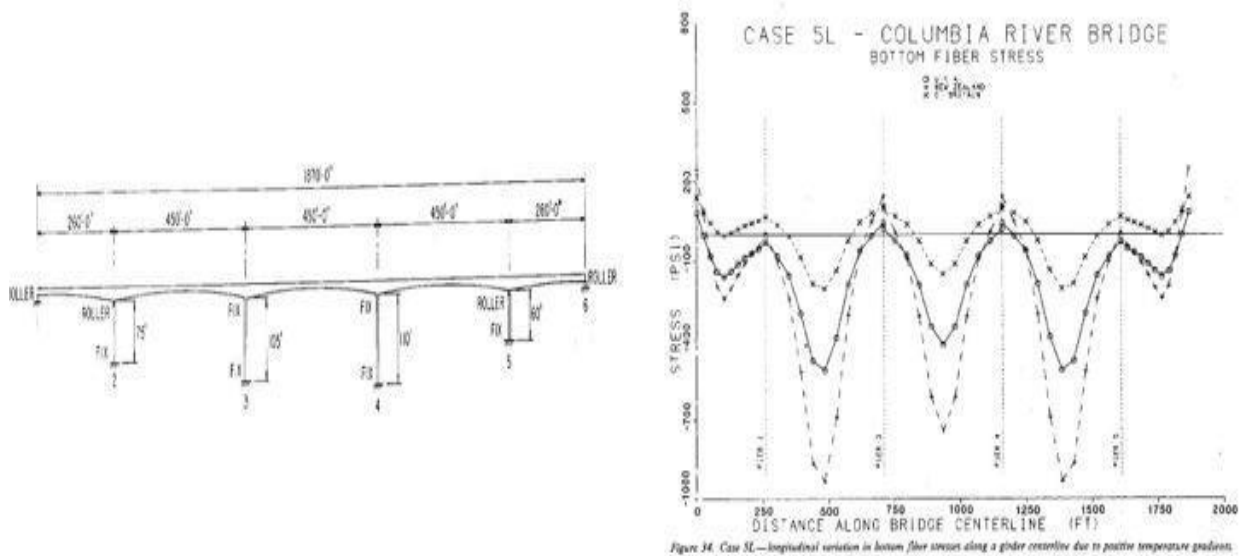


**Figure 7 Bottom Fiber stress values for hunched girder bridge**

***i. Proposed Thermal Gradient***

The thermal gradient proposed by this report was derived from the New Zealand thermal gradient. The shape was simplified from 5th order curve to three-line segments. It divided the country into four zones. Each zone was provided with three temperatures to form the thermal gradient.

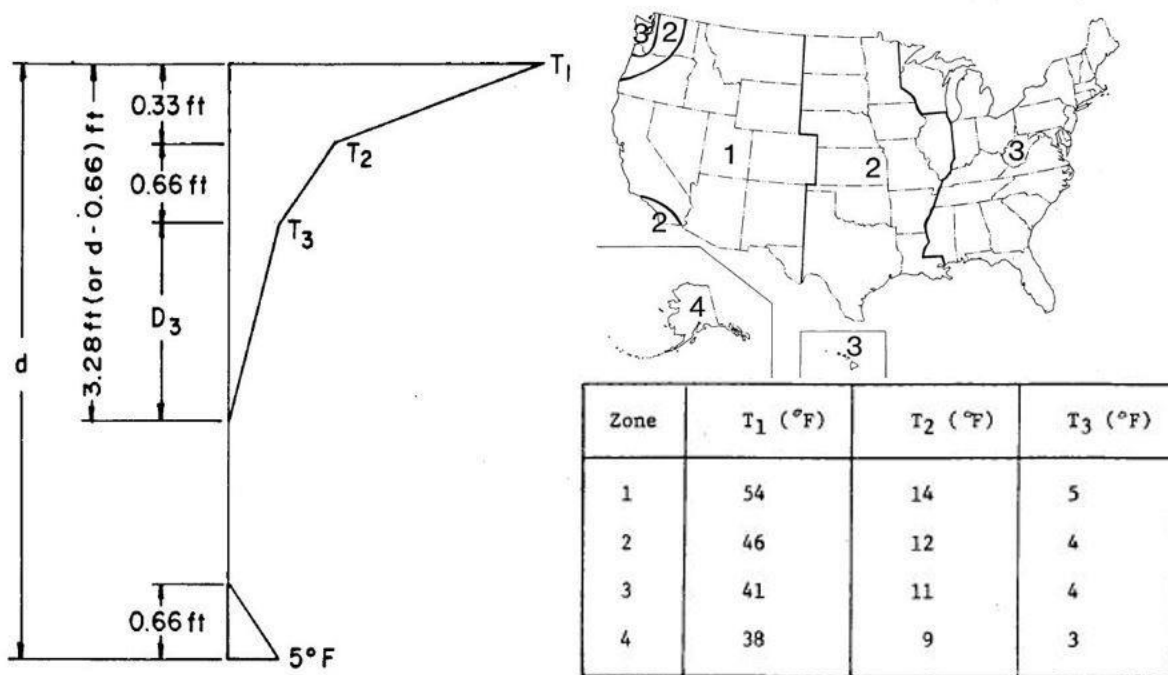
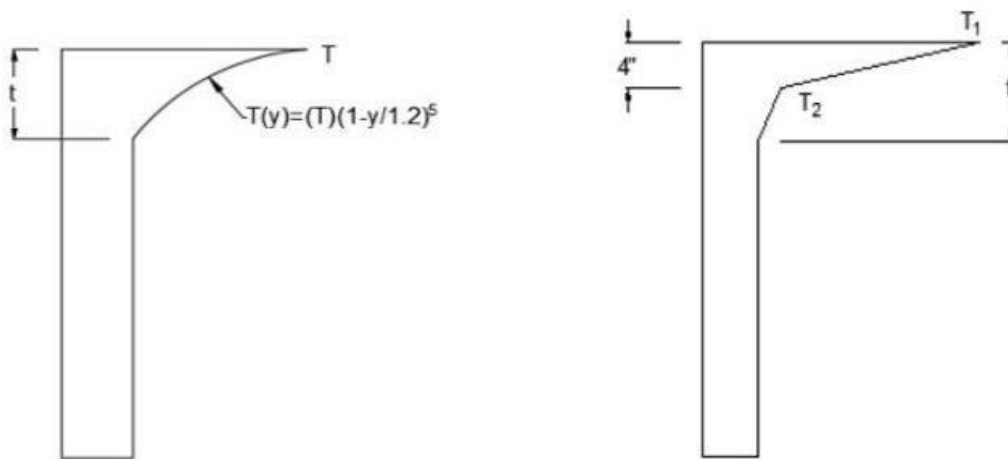


**Figure 8 Proposed Thermal Gradient for Concrete Superstructures**

This gradient with slight modification was taken and incorporated in the AASHTO specifications which is discussed in the next section.

***c. Australian Design Codes (AUSTROADS, 1992)***

The thermal gradient for steel bridges was derived from the gradient which is used in AUSTROADS 1992. This gradient is a fifth order curve that goes up to the steel-concrete interface and then has a uniform temperature throughout the girder. The simplifications made to this gradient are the transformation of the 5th order curve into simple line segments which are similar to the NCHRP report 276 for concrete superstructure.



-AUSTRROADS steel thermal gradient -AASHTO LRFD steel design thermal gradient

**Figure 9 AUSTRROADS VS AASHTO Thermal gradient for steel bridges**

The proposed gradients from NCHRP Report 276 for concrete bridges and AUSTRROADS 1992 for steel bridges are combined and provided in the present AASHTO specifications.

### 3. COMPARISON OF ALL THERMAL GRADIENTS

The below graph shows all the thermal gradients. All the 3 gradients, AASHTO Steel, AASHTO Concrete and Proposed NCHRP (Report 276, 1985) follow the same path up to the steel and concrete interface. After the interface the temperature throughout the steel girder is the same whereas they vary in other gradients.

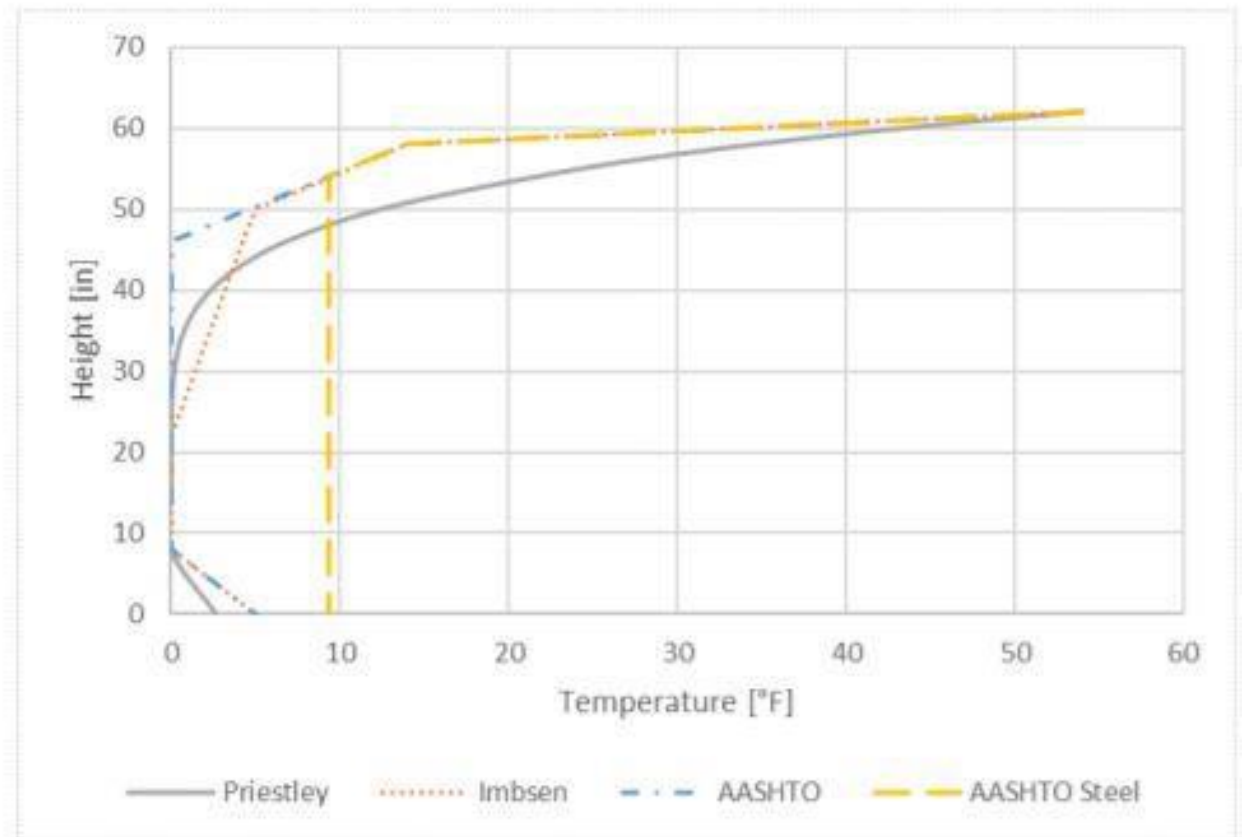


**Figure 10 Comparison of thermal gradients**

#### **4. AASHTO DESIGN CRITERION**

AASHTO LRFD Bridge Design specifications provides us with methods to calculate the bridge temperatures and the thermal deformations. The thermal loads are divided into two categories. The first effect is due to the uniform temperature change and other is effects due to thermal gradient along the depth of the bridge.

##### *a. Uniform Temperature change*

The temperature of the whole bridge is considered uniform across the depth and length. Uniform temperature change will cause expansions and contractions due

to positive and negative temperature change. The temperature at which the bridge was constructed is known as the setting temperature. During summer if the temperature of the bridge goes above the setting temperature then the bridge will expand because of the positive temperature difference while during winter the temperature goes below the setting temperature causing a negative temperature difference resulting in contraction. The ranges of temperature that need to be considered for several types of bridges and regions are specified in section AASHTO 3.12.2. There are two methods to calculate the thermal movements caused by uniform temperature difference.

**Procedure A:**

This is the historic procedure used for the calculation of thermal movements in the bridge design. This procedure provides us with the upper ( $T_{MaxDesign}$ ) and lower ( $T_{MinDesign}$ ) boundaries of the temperature and the base construction temperature that is assumed in the design shall be used. The 11 states are not divided in the US. The climates are differentiated according to the number of freezing days. Freezing days are defined as days where the average temperature is less than the 32°F. If the total number of freezing days are less than 14 per year then the location comes into moderate climate. If the number of freezing days is greater than 14 then the climate is cold. This procedure can be applied to all bridges unlike procedure B. The bridges are divided into 3 types steel, concrete and wood. The following table provides us with the maximum and minimum temperatures for several types of bridges in different climates.

### PROCEDURE A TEMPERATURE RANGES

Climate	Steel or Aluminum	Concrete	Wood
Moderate	0° to 120° F	10° to 80°F	10° to 75°F
Cold	-30° to 120°F	0° to 80°F	0° to 75°F

#### Procedure B:

This procedure was developed in 2002 based on the NCHRP report (NCHRP 20-07/106) written by Charles Roeder. This procedure uses Contour maps to obtain the  $T_{MaxDesign}$  and  $T_{MinDesign}$  depending upon the type of the bridge and its location. Two methods were used to construct these design maps. Kuppa and Emerson methods have been used to calculate the average maximum and minimum bridge temperatures. It was found that the Kuppa method provided better estimates in average bridge temperature. Hence the Kuppa method was combined with the historical weather data to produce the contour design maps. These are the maps that we use in procedure B. This procedure can be only applied to certain type of bridges. It can be applied to concrete girder bridges with concrete decks and steel girder bridges with concrete decks. There are a total of 4 contour maps for bridges which will provide  $T_{MaxDesign}$  and  $T_{MinDesign}$  for bridges with concrete girder and concrete decks and steel girders with concrete decks.

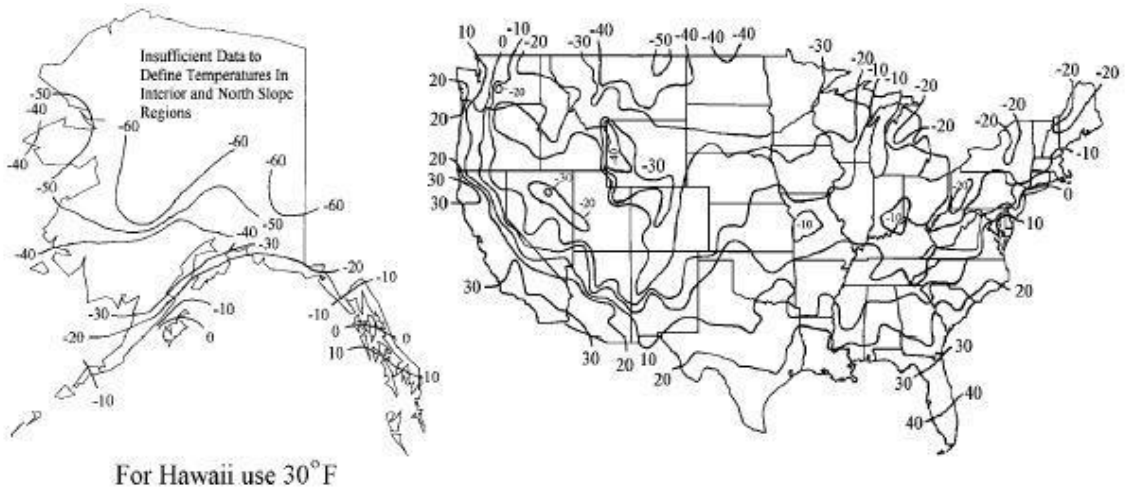
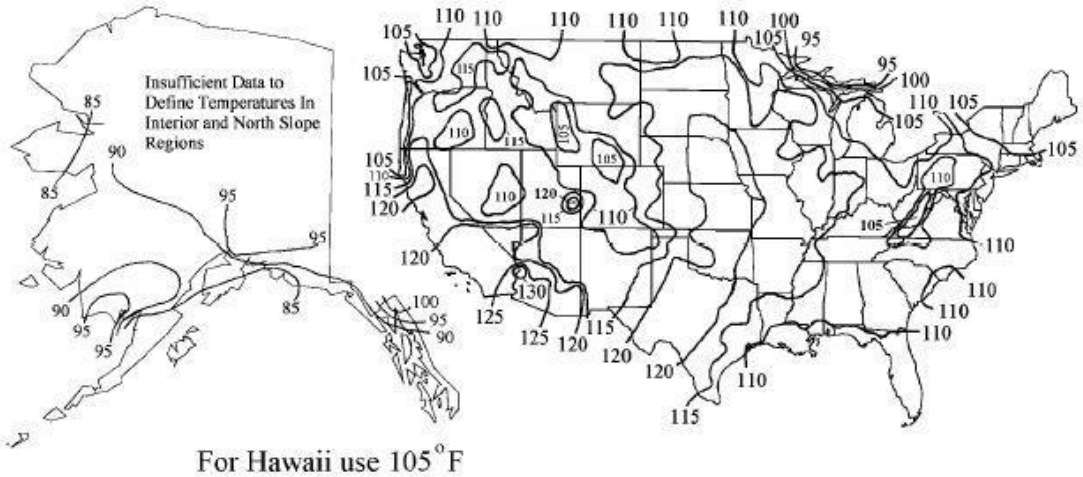


**Figure 11 Contour Maps for TMaxDesign and TMinDesign for Steel Girder Bridges with Concrete Decks**

The value closest to the contour can be taken or the value can be found out by linear interpolation between the two contour lines adjacent to the location of the bridge.

Maximum temperature maps have an increment of 5°F while the minimum temperature maps have an increment of 10°F.

### Calculation of Design Thermal Movements:

After obtaining the  $T_{MaxDesign}$  and  $T_{MinDesign}$  from either procedure A or Procedure B we use them to calculate the design thermal movements using the following formula

$$\Delta T = \alpha L (T_{MaxDesign} - T_{MinDesign})$$

Where

L = Span of the bridge (in.)

$\alpha$  = Coefficient of thermal expansion (in./in./°F)

These design thermal movements are used to design bearings and expansion joints. The present AASHTO specification doesn't provide any instructions for calculating the installation temperatures of bearings and expansion joints. NCHRP report recommends including the installation temperature of bearings and expansion joints in the design criterion for bridges. It provides us with the formula to calculate the installation temperature and then calculate the design thermal movements.

Installation Temperature and Design Movements for the following:

#### Elastomeric Bearing Pads:

$$T_{install} = T_{MinDesign} + 0.65 * (T_{MaxDesign} - T_{MinDesign})$$

$$\Delta = + \alpha L 0.65 * (T_{MaxDesign} - T_{MinDesign})$$

#### Other Bearings:

$$T_{install} = T_{MinDesign} + 0.5 * (T_{MaxDesign} - T_{MinDesign})$$

$$\Delta = + \alpha L (T_{MaxDesign} - T_{MinDesign} + 20^{\circ}F)$$

**Expansion Joints:**

$$T_{Install} = (T_{MaxAir} + T_{MinAir}) / 2$$

$$\Delta = \alpha L (T_{MaxDesign} - T_{MinDesign} + 30^{\circ}\text{F})$$

***b. Thermal Gradient***

This gives us the variation of temperature along the depth of the bridge section. The country is divided into four zones depending upon the solar radiation with each having different values for temperature gradient. The variation of the temperature is given in the figure and the values of T<sub>1</sub> and T<sub>2</sub> are provided in the table.

The current thermal gradient is derived from the NCHRP 276 (1985) report and the Australian design codes (AUSTROADS, 1992). The thermal gradient for concrete structures was taken from the NCHRP 276 report (1985) while the thermal gradient for steel bridges was taken from the Australian design codes (AUSTROADS, 1992).

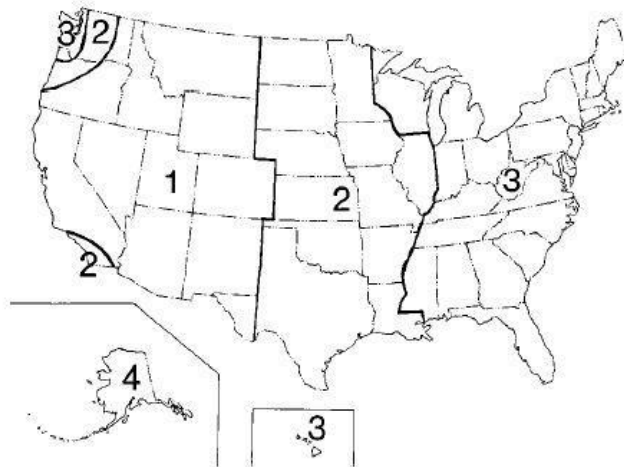


**Figure 12 Solar Radiation Zones for the United States**

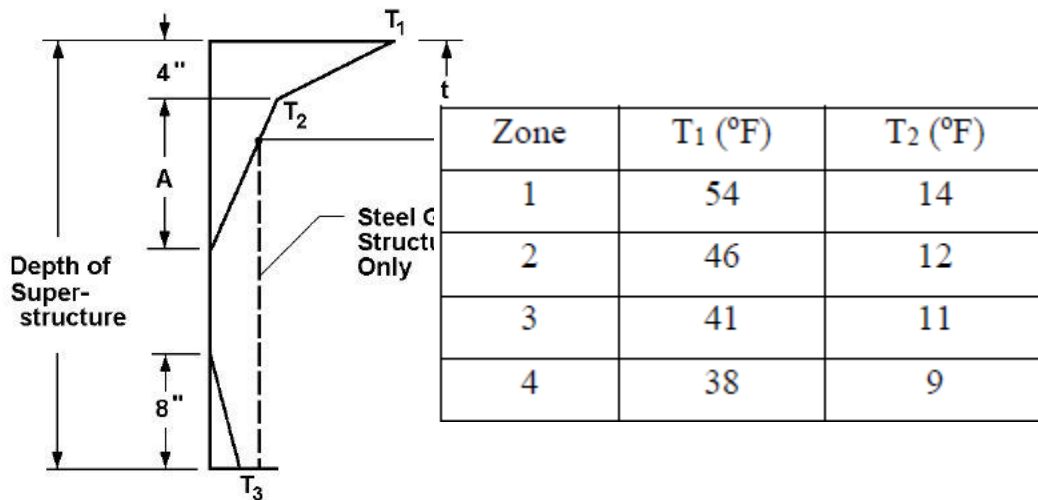


**Figure 13 Positive Vertical Temperature gradient in Concrete and Steel Superstructures**

T<sub>3</sub> will be taken as 0°F unless an accurate value is determined and should not exceed 5°F. For negative thermal gradient we multiply the values for the positive gradient by a factor of -0.3 for concrete decks.

**End of Section**

## Bibliography

- Kewalramani, M. A., Mohamed, O. A., & Syed, Z. I. (2017). Engineered Cementitious Composites for Modern Civil Engineering Structures in Hot Arid Coastal Climatic Conditions. *Procedia Engineering*, 180, 767-774. doi:10.1016/j.proeng.2017.04.237
- Caner, A., & Zia, P. (1998). Behavior and Design of Link Slabs for Jointless Bridge Decks. *PCI Journal*, 43(3), 68-80. doi:10.15554/pcij.05011998.68.80
- Au, A., Lam, C., Au, J., & Tharmabala, B. (2013). Eliminating Deck Joints Using Debonded Link Slabs: Research and Field Tests in Ontario. *Journal of Bridge Engineering*, 18(8), 768-778. doi:10.1061/(asce)be.1943-5592.0000417
- Li, V. (2008). Engineered Cementitious Composite (ECC). *Concrete Construction Engineering Handbook*. doi:10.1201/9781420007657.ch24
- Ulku, E., Attanayake, U., & Aktan, H. (2009). Jointless Bridge Deck with Link Slabs. *Transportation Research Record: Journal of the Transportation Research Board*, 2131(1), 68-78. doi:10.3141/2131-07
- Wing, K. M., & Kowalsky, M. J. (2005). Behavior, Analysis, and Design of an Instrumented Link Slab Bridge. *Journal of Bridge Engineering*, 10(3), 331-344. doi:10.1061/(asce)1084-0702(2005)10:3(331)
- Gunes, O., Yesilmen, S., Gunes, B., & Ulm, F. (2012). Use of UHPC in Bridge Structures: Material Modeling and Design. *Advances in Materials Science and Engineering*, 2012, 1-12. doi:10.1155/2012/319285
- Su, Y., Li, J., Wu, C., Wu, P., & Li, Z. (2016). Effects of steel fibres on dynamic strength of UHPC. *Construction and Building Materials*, 114, 708-718. doi:10.1016/j.conbuildmat.2016.04.007
- Abbas, S., Nehdi, M. L., & Saleem, M. A. (2016). Ultra-High Performance Concrete: Mechanical Performance, Durability, Sustainability and Implementation Challenges. *International Journal of Concrete Structures and Materials*, 10(3), 271-295. doi:10.1007/s40069-016-0157-4

- ASTM, *standard test method for flexural strength of concrete (using simple beam with third-point loading)*. Designation: C78/C78M—18. ASTM International, 2018.
- ASTM, *Standard Test Method for Flexural Properties of Unreinforced and Reinforced Plastics and Electrical Insulating Materials by Four-Point Bending*. Designation: D6272—17. ASTM International, 2018.
- Kato, H., Tottori, Y., & Sasaki, K. (2013). Four-Point Bending Test of Determining Stress-Strain Curves Asymmetric between Tension and Compression. *Experimental Mechanics*, 54(3), 489-492. doi:10.1007/s11340-013-9791-9
- Chen, L., & Graybeal, B. A. (2012). Modeling Structural Performance of Ultrahigh Performance Concrete I-Girders. *Journal of Bridge Engineering*, 17(5), 754-764. doi:10.1061/(asce)be.1943-5592.0000305
- Keoleian, G. A., Kendall, A., Dettling, J. E., Smith, V. M., Chandler, R. F., Lepech, M. D., & Li, V. C. (2005). Life Cycle Modeling of Concrete Bridge Design: Comparison of Engineered Cementitious Composite Link Slabs and Conventional Steel Expansion Joints. *Journal of Infrastructure Systems*, 11(1), 51-60. doi:10.1061/(asce)1076-0342(2005)11:1(51)
- Şahmaran, M., & Li, V. C. (2010). Engineered Cementitious Composites. *Transportation Research Record: Journal of the Transportation Research Board*, 2164(1), 1-8. doi:10.3141/2164-01
- Komatineni, N. (2017). Thermal Analysis of Steel Bridges (Scholarly Paper). University of Maryland, College Park, Maryland.